pharmaceutics

MDPI

Article

pH-Responsible Doxorubicin-Loaded Fe_3O_4@$CaCO_3$ Nanocomposites for Cancer Treatment

Victoriya Popova, Yuliya Poletaeva, Alexey Chubarov * and Elena Dmitrienko *

Institute of Chemical Biology and Fundamental Medicine, SB RAS, 8 Lavrentiev Avenue, 630090 Novosibirsk, Russia

* Correspondence: chubarov@niboch.nsc.ru or chubarovalesha@mail.ru (A.C.); elenad@niboch.nsc.ru (E.D.); Tel.: +7-913-763-1420 (A.C.); +7-913-904-1742 (E.D.)

Abstract: A magnetic nanocomposite (MNC) is an integrated nanoplatform that combines a set of functions of two types of materials. A successful combination can give rise to a completely new material with unique physical, chemical, and biological properties. The magnetic core of MNC provides the possibility of magnetic resonance or magnetic particle imaging, magnetic field-influenced targeted delivery, hyperthermia, and other outstanding applications. Recently, MNC gained attention for external magnetic field-guided specific delivery to cancer tissue. Further, drug loading enhancement, construction stability, and biocompatibility improvement may lead to high progress in the area. Herein, the novel method for nanoscale Fe_3O_4@$CaCO_3$ composites synthesis was proposed. For the procedure, oleic acid-modified Fe_3O_4 nanoparticles were coated with porous $CaCO_3$ using an ion coprecipitation technique. PEG-2000, Tween 20, and DMEM cell media was successfully used as a stabilization agent and template for Fe_3O_4@$CaCO_3$ synthesis. Transmission electron microscopy (TEM), Fourier transform infrared (FTIR) spectroscopy, and dynamic light scattering (DLS) data were used for the Fe_3O_4@$CaCO_3$ MNC's characterization. To improve the nanocomposite properties, the concentration of the magnetic core was varied, yielding optimal size, polydispersity, and aggregation ability. The resulting Fe_3O_4@$CaCO_3$ had a size of 135 nm with narrow size distributions, which is suitable for biomedical applications. The stability experiment in various pH, cell media, and fetal bovine serum was also evaluated. The material showed low cytotoxicity and high biocompatibility. An excellent anticancer drug doxorubicin (DOX) loading of up to 1900 μg/mg (DOX/MNC) was demonstrated. The Fe_3O_4@$CaCO_3$/DOX displayed high stability at neutral pH and efficient acid-responsive drug release. The series of DOX-loaded Fe_3O_4@$CaCO_3$ MNCs indicated effective inhibition of Hela and MCF-7 cell lines, and the IC 50 values were calculated. Moreover, 1.5 μg of the DOX-loaded Fe_3O_4@$CaCO_3$ nanocomposite is sufficient to inhibit 50% of Hela cells, which shows a high prospect for cancer treatment. The stability experiments for DOX-loaded Fe_3O_4@$CaCO_3$ in human serum albumin solution indicated the drug release due to the formation of a protein corona. The presented experiment showed the "pitfalls" of DOX-loaded nanocomposites and provided step-by-step guidance on efficient, smart, anticancer nanoconstruction fabrication. Thus, the Fe_3O_4@$CaCO_3$ nanoplatform exhibits good performance in the cancer treatment area.

Keywords: iron oxide and calcium carbonate nanoparticles; Fe_3O_4@$CaCO_3$; nanocomposites; magnetic nanocomposites; drug delivery; doxorubicin; human serum albumin; pH-sensitive drug release; cancer treatment; toxicity

Citation: Popova, V.; Poletaeva, Y.; Chubarov, A.; Dmitrienko, E. pH-Responsible Doxorubicin-Loaded Fe_3O_4@$CaCO_3$ Nanocomposites for Cancer Treatment. *Pharmaceutics* **2023**, *15*, 771. https://doi.org/10.3390/pharmaceutics15030771

Academic Editors: Elena V. Uspenskaya and Anton V. Syroeshkin

Received: 31 January 2023
Revised: 17 February 2023
Accepted: 23 February 2023
Published: 26 February 2023

1. Introduction

Magnetic nanocomposites (MNCs) combine the properties of magnetic nanoparticles (MNPs) and a second material, yielding a broad range of properties of the two phases. Moreover, such incorporation gives a new unique feature, providing widespread applications. The building blocks for MNCs may be organic molecules or polymers, inorganic substances, and bioinspired [1–3].

MNCs have widespread applications in drug delivery, magnetic field-influenced transport, magnetic resonance imaging, hyperthermia therapy, theranostics, magnetic separation, and biosensor areas [4–29]. NC is a promising tool for external magnetic field target-specific delivery of anticancer agents [1,21,22,30]. The surfaces of MNPs for in vivo applications should be modified with a highly biocompatible material to acquire excellent stability, good solubility, and low toxicity [1]. The good magnetic core surface protection and low interaction with a solvent primarily lead to high biocompatibility of MNPs [2,3,31–34]. The core–shell structure of MNCs is generally well tolerated in vivo [25,35–38]. It provides tunable properties, easy surface functionalization, and low toxicity [25,35–38].

Calcium carbonate ($CaCO_3$) is a well-known mineral applied in various biocompatible materials [39–44]. $CaCO_3$ is the cheapest inorganic coating with a porous structure, pH-sensitive drug loading and release, and high stability [40–42,45]. Recently, we have fabricated nanoscale porous, anticancer drug-loaded $CaCO_3$ that showed excellent A549 cell inhibition [41]. Moreover, $CaCO_3$ nanoparticles exhibit weak acid decomposition, which can be found in the cancer microenvironment and endosomal compartment, facilitating drug release in tumors [39–41]. Hence, the magnetic core/inorganic shell hybrid nanocomposite possesses remarkable priority over other MNCs. Recently, Fe_3O_4@$CaCO_3$ nanocomposites were designed for metal ions, dyes, magnetic cell separation, enzyme immobilization, and drug adsorption [46–56]. However, only few works show the possible therapeutic applications of Fe_3O_4@$CaCO_3$ [50]. Despite the advantages, Fe_3O_4@$CaCO_3$ production is a complex and less-reproducible task. Moreover, the previously synthesized nanocomposites larger than 200 nm form an aggregate. The lower nanoparticle sizes are more suitable for therapeutic applications.

Doxorubicin (DOX) is an outstanding anticancer drug [57–59]. The DOX loading on nanoparticles' surface serves as a prospective system that reduces side effects and avoids drug resistance problems [41,58–65]. Therefore, it is essential to develop new pH-stimuli-responsive DOX-released multifunctional constructions based on MNCs [66–68]. Moreover, for further in vivo studies, the excellent capacity of DOX is required. The DOX-loaded MNCs should be stable at a plasma pH of ~7.4 and enable efficient drug release in cancer tissue (pH of 5–5.5) [45,64,66,69–71].

Herein, we reported a novel reproducible synthesis of inorganic Fe_3O_4@$CaCO_3$ nanocomposites with a size of less than 200 nm for biomedical applications. To improve the nanocomposite properties, the concentration of the magnetic core was varied, yielding optimal size, polydispersity, and aggregation ability while maintaining the magnetic properties. The prepared MNCs morphology and aggregation were analyzed using transmission electron microscopy (TEM), Fourier transform infrared (FTIR) spectroscopy, and dynamic light scattering (DLS). The stability experiments of Fe_3O_4@$CaCO_3$ nanocomposites in acetate buffer (pH 5.0, 7.0), PBS buffer (pH 7.4), DMEM cell media, and 10% fetal bovine serum (FBS) were studied. To serve as a drug carrier, the DOX loading capacity and pH-dependent release kinetic profile were investigated. For this, a series of DOX-loaded Fe_3O_4@$CaCO_3$ was synthesized. This method provides a high DOX capacity of up to 1900 μg/mg (DOX/MNPs) with 34% loading efficiency or a low capacity of 25 μg/mg with 80% efficiency. The Fe_3O_4@$CaCO_3$/DOX nanocomposites indicate high pH stability in neutral pH and efficient drug release in acidic media. For Fe_3O_4@$CaCO_3$/DOX series, the cytotoxicity on HeLa and MCF-7 cell lines was tested. The systemic experimental results per DOX concentration or nanoparticle amount allowed the proof-of-concept of nanocomposite contribution to drug-resistance cancer treatment. The stability experiments with human serum albumin solution in physiological concentration showed the "pitfalls" of DOX-loaded nanocomposites and provided step-by-step guidance on efficient, smart, anticancer nanoconstruction fabrication. We believe that the presented work will bring new quality to the targeted drug delivery area.

2. Materials and Methods

2.1. Materials

$FeCl_2 \cdot 4H_2O$ (97–102%), $FeCl_3 \cdot 6H_2O$ (97–102%), and sodium acetate (99.9%) were obtained from PanReac AppliChem (Barcelona, Spain). Sodium bicarbonate (≥99.7%), calcium chloride, magnesium chloride, oleic acid, boric acid, phosphate-buffered saline (PBS), and Tween 20 were purchased from Sigma (St. Louis, MO, USA). Polyethylene glycol 2000 was obtained from Carl Roth (Karlsruhe, Germany). Doxorubicin was acquired from Ferein (Moscow, Russia). 3-(4,5-Dimethyl-2-thiazolyl)-2,5-diphenyl-2H-tetrazolium bromide (MTT) was purchased from Panreac Química (Barcelona, Spain). Fetal bovine serum (FBS), DMEM (Dulbecco's modified Eagle medium), GlutaMax, and antimycotic antibiotic solution were obtained from GIBCO, Life Technologies (Carlsbad, CA, USA). Human serum albumin (HSA) was purchased from Renal Laborvegyszer Kereskedelmi Kft. (Budapest, Hungary). Deionized water (Milli-Q) was used to prepare solutions.

2.2. Characterization of NPs

Dynamic light scattering (DLS) and zeta potential (ζ-potential) measurements were carried out on Malvern Zetasizer Nano (Malvern Instrument Ltd., Worcestershire, UK). For DLS studies, Fe_3O_4@$CaCO_3$ was diluted in deionized water to a concentration of 100 μg/mL. Transmission electron microscopy (TEM) images were obtained on a JEM-1400 (Jeol, Tokyo, Japan). Images were captured using a side-mounted Veleta digital camera (EM SIS, Muenster, Germany). UV-vis spectra were recorded on a UV-2100 spectrophotometer (Shimadzu, Kyoto, Japan) and microplate reader Clariostar (BMG, Ortenberg, Germany). FTIR spectra were measured on a 640-IR FT-IR spectrometer (Varian, MA, USA) from 4000 to 400 cm^{-1} at room temperature accompanied with a KBr pellet.

2.3. Fe_3O_4@$CaCO_3$ Nanocomposite Synthesis

The synthesis of oleic acid-coated Fe_3O_4 nanoparticles was adapted from Kovrigina et al. and Wang et al. [72,73]. Briefly, the 0.28 g $FeCl_3 \cdot 6H_2O$ (1 mmol) and 0.1 g $FeCl_2 \cdot 4H_2O$ (0.5 mmol) were dissolved in 10 mL of HCl (1 M) and heated at 85 °C. Afterward, 95 μL of oleic acid (0.3 mmol) in acetone was added dropwise and stirred (750 rpm) at 85 °C for 5 min. After the incubation, 2 mL of NaOH (8 M) was added up to pH 11.0 under stirring (750 rpm) at 85 °C for 30 min. The mixture was cooled to room temperature. Afterward, 9 mL of HCl (1 M) was added up to pH 2.0. The obtained magnetite nanoparticles were collected using a magnet and washed with 1.0 mL of acetone (three times), and 1.0 mL of deionized water (three times). The nanoparticles were redispersed in deionized water and stored at room temperature.

Fe_3O_4@$CaCO_3$ nanocomposites were adapted from Popova et al. [41]. Briefly, 0.45–4.5 mg Fe_3O_4 and 0.1 g polyethylene glycol 2000 were dissolved in 0.8 mL of deionized water. To the resulting mixture, 0.1 mL of sodium bicarbonate (1 M), 0.1 mL of Tween 20 (20 vol. %), and 0.1 mL of DMEM were added. The 0.1 mL solution, which contains 0.010 mL of calcium chloride (0.1 M), 0.010 mL of magnesium chloride (0.1 M), and 0.010 mL of DMEM, was added slowly under sonification in an ultrasonic bath for 2 min. The mixture was stirred at 25 °C for 20 min (750 rpm). Finally, Fe_3O_4@$CaCO_3$ was collected using a magnet and redispersed in deionized water. The brown magnetic suspension was kept in deionized water at 23−25 °C.

2.4. Fe_3O_4@$CaCO_3$ Stability

The stability of 100 μg Fe_3O_4@$CaCO_3$ was analyzed in 1 mL of 100 mM acetate buffer (pH from 5.0 to 6.0), 10 mM PBS (pH 7.4), DMEM, and 10% fetal bovine serum at 25 °C under stirring (750 rpm). At various time points, the aliquot of the solution was collected, followed by re-mixing. The aliquots were analyzed using DLS.

2.5. Doxorubicin-Loaded Fe_3O_4@$CaCO_3$ Synthesis

Briefly, 0.025–3.2 mg Fe_3O_4@$CaCO_3$ was redispersed in 0.8 mL of deionized water. The 0.1 mL of DOX (100 μg, 1 mg/mL) and 0.1 mL of sodium borate buffer pH 8.0 (10 mM) were added. The mixture was incubated at 25 °C for 12 h under stirring (750 rpm). The nanoparticles were collected using a magnet, washed with sodium borate buffer pH 8.0 (10 mM) three times, and redispersed in sodium borate buffer pH 8.0 (10 mM). The concentration of DOX in the supernatant was determined spectrophotometrically (λ = 480 nm). The amount of the loaded drug was determined as a capacity using the equation: $E = (DOX_0 - DOX)/N$. The DOX_0 and DOX represent the initial and the discard solution amount of DOX (μg), respectively. N denotes the amount of Fe_3O_4@$CaCO_3$ (mg).

2.6. Doxorubicin Release from Fe_3O_4@$CaCO_3$

The release of DOX was investigated at 25 °C in 1 mL of 100 mM sodium acetate buffer (pH of 4.0 to 6.0) or 10 mM phosphate-buffered saline (pH 7.4) containing Fe_3O_4@$CaCO_3$ (variable amount of DOX with 0.1 mg of Fe_3O_4@$CaCO_3$) with constant stirring (750 rpm). The amount of DOX released into the solution was determined using the optical density of the solution at different time points.

2.7. Human Serum Albumin and Fe_3O_4@$CaCO_3$/DOX Interactions

To the solution of human serum albumin (HSA, 0.8–32 mg) in PBS (1.0 mL), Fe_3O_4@$CaCO_3$/DOX (0.1 mg) was added. The mixture was stirred (750 rpm) at 37 °C for 1, 4, 8, and 24 h. The Fe_3O_4@$CaCO_3$/DOX nanocomposites coated with HSA were collected using a magnet and redispersed in deionized water. The concentration of the released DOX and HSA were measured spectrophotometrically.

2.8. The Cytotoxicity Assay (MTT Test)

Tumor cell lines from human mammary adenocarcinoma MCF-7 and cervical cancer HeLa (Russian Branch of the ETCS, St. Petersburg, Russia) were plated in 96-well culture plates (5×10^3 cells per well) in DMEM medium supplemented with 10% FBS, 1% GlutaMax, and 1% antimycotic antibiotic solution at 37 °C and 5% CO_2 for 24 h.

The cytotoxicity studies were performed using a colorimetric assay based on the cleavage of 3-[4,5-dimethylthiazol-2-yl]-2,5-diphenyl-tetrazolium bromide (MTT) by mitochondrial dehydrogenases in viable cells, leading to a blue precipitate of formazan formation [74]. The cells were supplemented with media containing Fe_3O_4@$CaCO_3$ (0.2–2000 μg/mL), Fe_3O_4@$CaCO_3$/DOX (0.9–73.4 μg/mL), DOX (0.1–10.0 μM) for 48 h at 37 °C and 5% CO_2. The cells incubated with the medium were used as a control. After incubation, the medium was removed, and 200 μL of MTT solution (0.25 mg/mL in the culture medium containing 1% of antimycotic antibiotic solution) was added and incubated for 4 h under the same conditions. Afterward, the medium was removed, and formazan was dissolved in 0.1 mL of DMSO. The optical density was measured on a multichannel plate reader Clariostar at 570 nm (peak). The percentage of surviving cells was calculated from the obtained optical density as a percentage of the control values. The half-maximal inhibitory concentration (IC 50) was calculated graphically. All measurements were repeated not less than three times with a standard deviation calculation.

3. Results and Discussion

3.1. Synthesis and Characterization of Fe_3O_4@$CaCO_3$

Nanoparticles can accumulate and be retained in tumors from circulating blood due to the enhanced permeability and retention (EPR) effect. However, the optimal size of the nanoparticles should be lower than 150–200 nm to penetrate through vascular structures. On the contrary, nanoparticles smaller than 10–20 nm are rapidly cleared by renal filtration. In this way, this work aimed to synthesize the nanocomposites with optimal size. The synthesis of Fe_3O_4@$CaCO_3$ nanocomposites was carried out in a two-step procedure by the production of the magnetite core with subsequent carbonate coating (Figure 1). Magnetic

iron oxide nanoparticles were synthesized using the classical co-precipitation method. The procedure consists of Fe^{2+}/Fe^{3+} salts and surfactant co-precipitation in the presence of the base (see Section 2.3). The widely used surfactant, oleic acid, was chosen for nanoparticle stabilization, allowing high saturation magnetization value [72,75–77].

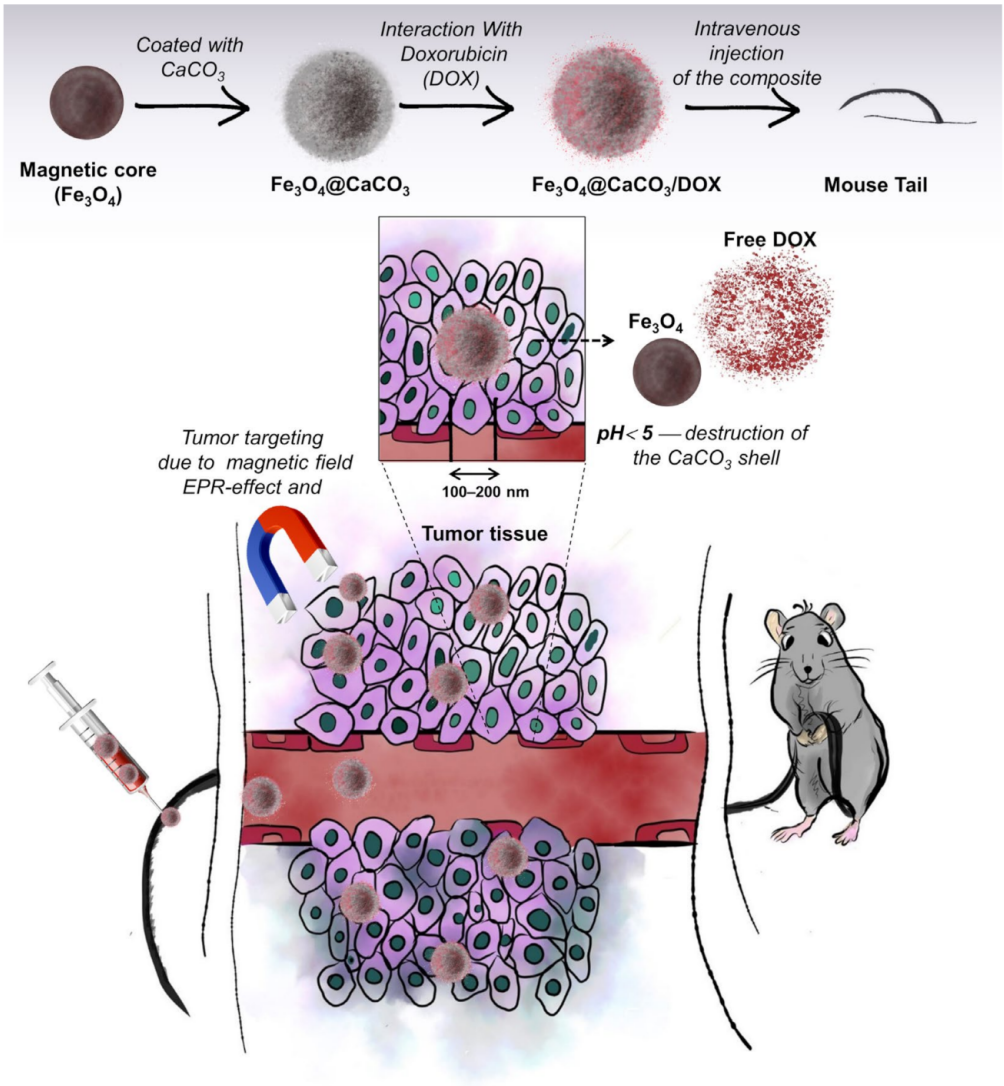

Figure 1. Synthesis of Fe_3O_4@$CaCO_3$ and doxorubicin-loaded (Fe_3O_4@$CaCO_3$/DOX) nanocomposites and their distribution through the bloodstream to the tumors.

For $CaCO_3$ layer synthesis, our group's adapted previously published protocol was utilized [41]. The fabrication of small-sized, porous, and stable $CaCO_3$ nanoparticles is a difficult task [78]. Obtaining a stable suspension of calcium carbonate nanoparticles down to 200 nm is still a methodological challenge [41,78]. There are a few synthesis methods that produce magnetic Fe_3O_4@$CaCO_3$ hybrids with particle size higher than 1 µm [50–52,54]. Despite their disadvantages, nanoscale particles are required for drug delivery. Only two research groups presented the synthesis of Fe_3O_4@$CaCO_3$ nanocomposites as promising multifunctional drug delivery systems [47,49]. In the present work, the mixture of stabilization agents such as polyethylene glycol 2000 (PEG 2000) and Tween 20 in the presence of cell media DMEM was used to reduce the size and increase the stability and monodispersity of $CaCO_3$ nanoparticles. The novelty of our approach, apart from using the different compositions of the reaction mixture during the formation phase of the $CaCO_3$ layer, is that there is no need to stabilize the composite with additional coatings that alter its characteristics, including

sensitivity to pH and drug sorption. PEG-2000 and Tween 20 form a polymeric structure that serves as a template limiting particle growth during nucleation [41]. The amino acids, vitamins, and salts in DMEM presumably stabilize the nanoparticles. PEG-2000 and Tween 20 are well-known amphiphilic surfactants [79–81]. Moreover, PEGylation decreases the non-specific interactions with proteins, improves biocompatibility, and prolongs blood circulation time [79]. The obtained nanoscale Fe_3O_4 and Fe_3O_4@$CaCO_3$ were characterized by dynamic light scattering (DLS, Table 1) and transmission electron microscopy (TEM, Figure 2). For comparison, $CaCO_3$ nanoparticles were synthesized according to the same procedure [41].

Table 1. Diameter by DLS and TEM, PDI, and ζ-potential of Fe_3O_4 and $CaCO_3$ nanoparticles and different Fe_3O_4@$CaCO_3$ nanocomposites using a variable amount of magnetic core from 0.45 to 4.5 mg/mL for synthesis.

Initial Amount Fe_3O_4, μg/mL	Hydrodynamic Diameter by DLS, nm	Diameter by TEM, nm		PDI	ζ-Potential, mV	TEM Image (Figure 2)
		NP	Agglomerate			
4.5	130 ± 2	13 ± 2	107 ± 41	0.211 ± 0.006	−15.0 ± 0.3	C
1.8	118 ± 3	16 ± 2	68 ± 20	0.26 ± 0.01	−14.9 ± 0.3	D
0.9	130 ± 9	18 ± 3	61 ± 19	0.248 ± 0.004	−15.5 ± 0.4	E
0.45	121 ± 6	22 ± 1	—	0.31 ± 0.01	−15.6 ± 0.5	F
Initial Fe_3O_4	88 ± 5	11 ± 4	91 ± 23	0.221 ± 0.004	21.6 ± 0.7	A
Control $CaCO_3$	204 ± 8	26 ± 3	—	0.14 ± 0.02	−17.3 ± 0.4	B

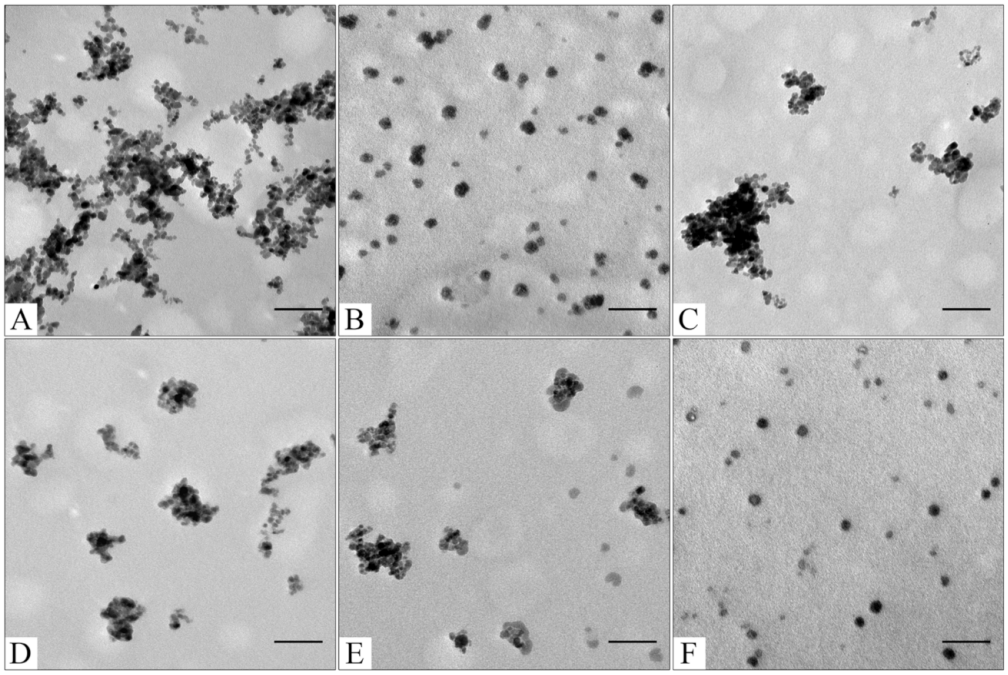

Figure 2. TEM images of sourced Fe_3O_4 (**A**); $CaCO_3$ (**B**); Fe_3O_4@$CaCO_3$ obtained using 4.5 mg/mL (**C**); 1.8 mg/mL (**D**); 0.9 mg/mL (**E**); 0.45 mg/mL of Fe_3O_4 (**F**). The bar indicates 100 nm.

To optimize the composition of the composite, the concentration of the magnetic core was varied from 0.45 to 4.5 mg/mL. All samples obtained had sufficient magnetic properties to allow magnetic separation to be applied in all stages of the operation (Figure 3). The surface charge, size, and morphology of nanoparticles are essential factors that influence cell and tissue internalization. Small nanoparticles (5–10 nm) have demonstrated high renal clearance. Large-sized nanoparticles (>200 nm) have a problem passing through cellular membranes [82]. The calculated mean particle diameters by TEM and DLS are summarized in Table 1. According to the DLS, Fe_3O_4@$CaCO_3$ nanocomposites have a comparable size of 120–130 nm, which is 30 nm higher than the initial Fe_3O_4 and optimal for drug delivery applications. However, the diameter of nanoparticles by TEM and DLS highly differ by

at least 1.5–2 times, which was previously found for $CaCO_3$ nanoparticles [45,49,83]. This phenomena is probably due to the aggregation and swelling occurring in water [83] and the water shell on the nanoparticle surface. Although a significant difference in the size and agglomeration of the nanocomposites can be seen visually on the TEM, the differences in the hydrodynamic diameter by DLS are insignificant. This is probably due to the greater propensity of particles with a high content of magnetite to aggregate during the preparation of samples for TEM [84]. Moreover, as the amount of Fe_3O_4 in the sample decreases, the proportion of carbonate component increases, and the degree of particle aggregation decreases (cf. Figure 2C–F), which is clearly expressed in Figure 2F. For further investigation, magnetic nanocomposite with the lowest Fe_3O_4 amount (0.45 μg/mL) and the highest carbonate component was chosen (Table 1, Figures 3F and S1). The high similarity between the TEM images of the selected sample (Figure 2F) and the pure $CaCO_3$ (Figure 2B) may indicate the absence of a magnetic core. However, the sample has enough magnetic properties, shown using easy magnetic separation in each step of the synthesis (Figure 3). The resulting Fe_3O_4@$CaCO_3$ nanocomposite has a size by DLS of 121 ± 6 nm (PDI = 0.31 ± 0.01) and ζ-potential (−15.6 ± 0.5 mV).

Figure 3. Magnetic separation of Fe_3O_4@$CaCO_3$ nanocomposite (0.45 mg/mL of Fe_3O_4 synthesis) immediately (**left**) and after 15 s (**right**).

To confirm the components of oleic acid-modified Fe_3O_4@$CaCO_3$ nanocomposites, the Fe_3O_4 nanoparticles, Fe_3O_4@$CaCO_3$, and Fe_3O_4@$CaCO_3$/DOX FTIR spectra were recorded, and the results were presented in Figure 4. The FTIR spectrum of oleic acid-coated Fe_3O_4 nanoparticles displayed the characteristic adsorption peaks of oleic acid and Fe_3O_4 core at 3421, 2918 (asymmetric -CH_2 stretch), 2854 (symmetric -CH_2 stretch), 1626 (-COO^- stretch), 1464 (O-H stretch in plane), and 584 cm^{-1} (Fe-O stretch) [55,85]. For Fe_3O_4@$CaCO_3$, the spectrum shows the same stretches and the appearance of new bands at 1464 (main asymmetric stretch with a shoulder), 1150 (symmetric stretch), 890 (out-of-plane bending), and ~750 cm^{-1} (in-plane bending), corresponding to CO_3^{2-} [55,86,87]. The nanocomposite stability in an aqueous media is an essential factor for biomedical applications. After the synthesis, Fe_3O_4@$CaCO_3$ retains stability in deionized water during storage at 7 °C for 5 months without significant changes in the size evaluated by DLS (Figure S2). The further stability of Fe_3O_4@$CaCO_3$ was analyzed in acetate buffer (pH 5.0, 6.0), PBS buffer (pH 7.4), DMEM, and 10% fetal bovine serum (FBS) using DLS (Figure S3). In acetate buffer (pH 5.0 and 6.0) and FBS, Fe_3O_4@$CaCO_3$ showed almost the same average size as the initial nanoparticles for at least one week (Figure S3). However, in PBS and DMEM, Fe_3O_4@$CaCO_3$ immediately resized from 121 nm to 370–390 and 850–890 nm, respectively. No changes occurred during one-week storage (Figure S3). After 8 days of incubation, Fe_3O_4@$CaCO_3$ nanoparticles were magnetically separated, resuspended in deionized water without sonification, and analyzed using DLS. The hydrodynamic

diameter of Fe_3O_4@$CaCO_3$ was 180 ± 7 nm (PBS) and 106 ± 7 nm (DMEM). Despite the slight changes in size, the material was still less than 200 nm, which is essential for biomedical applications.

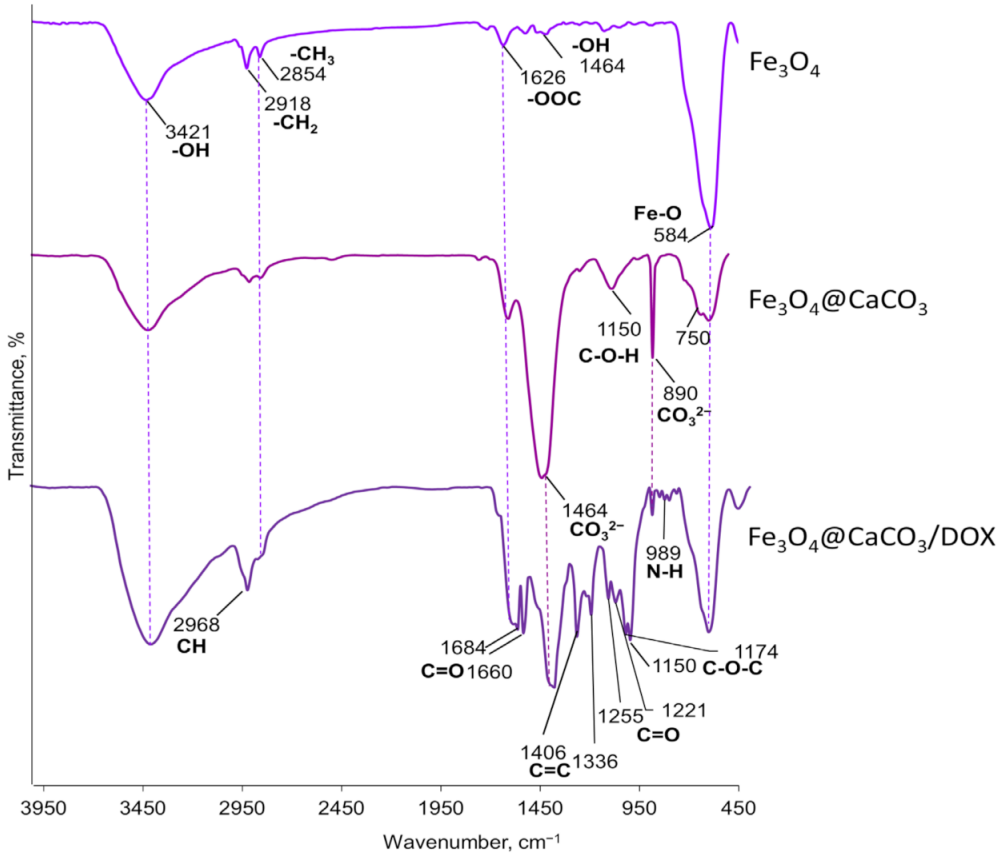

Figure 4. FTIR spectra of Fe_3O_4, Fe_3O_4@$CaCO_3$, and Fe_3O_4@$CaCO_3$/DOX nanocomposites.

3.2. Anticancer Drug Doxorubicin (DOX) Loading

The DOX loading efficiency onto the Fe_3O_4@$CaCO_3$ was studied using UV-vis spectroscopy (480 nm) and fluorescence. The optical density of the buffer solution with a drug was evaluated before and after loading, allowing the calculation of DOX capacity. According to the previously published procedure [41,72], the sodium borate buffer (10 mM, pH 8.0) was chosen for drug loading. The loading was carried out at 25 °C for 12 h. The drug loading on the nanocomposite may be easily seen in the photography as the appearance of red color during the separation procedure on the magnetic rack (Figure S6). The same qualitative data may be obtained by recording the fluorescence and UV-vis spectra of Fe_3O_4@$CaCO_3$/DOX nanocomposites (Figure S7). Moreover, Fe_3O_4@$CaCO_3$/DOX can be characterized using FTIR spectroscopy (Figure 4). The same peaks as for Fe_3O_4@$CaCO_3$ may be observed in the Fe_3O_4@$CaCO_3$/DOX spectrum (Figure 4). The drug-loading results in intensive specific adsorption peaks of DOX at 2968 (C–H stretch), 1684 (C=O stretch, quinone), 1660 (C=C ring stretch), 1406 (C–C), 1336, 1255, 1221 (=C–O–CH_3), and 1150 cm^{-1} [88,89].

The capacity was estimated as the amount of DOX bound to 1 mg of nanoparticles. By varying the initial particle concentration (from 0.025 to 3.2 mg/mL), capacity values from 25 to 1900 μg/mg (DOX/Fe_3O_4@$CaCO_3$) were obtained (Table 2, Figure 5). Figure 5 shows the dependence of Fe_3O_4@$CaCO_3$ capacity (μg/mg) and DOX loading efficiency (%) on nanoparticle concentration. It can be easily seen on the chart that a high Fe_3O_4@$CaCO_3$ concentration results in low capacity with a drug high loading efficiency. The graph has a linear relationship in the presented range of concentrations. For excellent drug-loading, a

low amount of nanocomposites and the same concentration of DOX are required. However, it is difficult to use such a low concentration of Fe_3O_4@$CaCO_3$ for Fe_3O_4@$CaCO_3$/DOX fabrication, which is expressed in the complexity of composites addition, increased procedure volumes, high consumption of the antibiotics, and the complexity of isolation due to the low efficiency of magnetic separation in high solution volume.

Table 2. Diameter by DLS and TEM, PDI, ζ-potential, and capacity of DOX-loaded nanocomposites Fe_3O_4@$CaCO_3$/DOX.

Fe_3O_4@$CaCO_3$ Amount, mg/mL	Hydrodynamic Diameter by DLS, nm	Diameter by TEM, nm			PDI	ζ-Potential, mV	Capacity, μg/mg	DOX Loading Efficiency, %	TEM Image Figure 6
		NP	Agglomerate	Shell					
3.2	133 ± 3		—		0.234 ± 0.005	−14.7 ± 0.7	25± 1	79.7 ± 0.2	—
1.6	130 ± 2		—		0.192 ± 0.008	−13.0 ± 0.2	45 ± 2	74.7 ± 0.1	—
1.0	128 ± 3	10 ± 2	75 ± 13	4.6 ± 0.3	0.144 ± 0.006	−18.8 ± 0.6	73.2 ± 0.4	73.2 ± 0.4	A
0.40	129 ± 3		—		0.130 ± 0.002	−14.9 ± 0.4	160 + 2	64.9 ± 0.6	—
0.20	135 ± 5	11 ± 3	125 ± 31	18 ± 2	0.14 ± 0.01	−15.0 ± 0.3	295 + 2	59.4 ± 0.3	B
0.10	111 ± 3	9 ± 3	149 ± 45	46 ± 9	0.30 ± 0.01	−16.5 ± 0.3	525 ± 3	52.4 ± 0.4	C
0.050	113 ± 5	9 ± 5	201 ± 35	158 ± 46	0.28 ± 0.03	−12.4 ± 0.2	1045 ± 10	45 ± 2	D
0.025	105 ± 3		—		0.29 ± 0.01	−19.0 ± 0.5	1900 ± 27	34 ± 4	—
Initial Fe_3O_4@$CaCO_3$	121 ± 6		—		0.31 ± 0.01	−15.6 ± 0.5	—	—	—

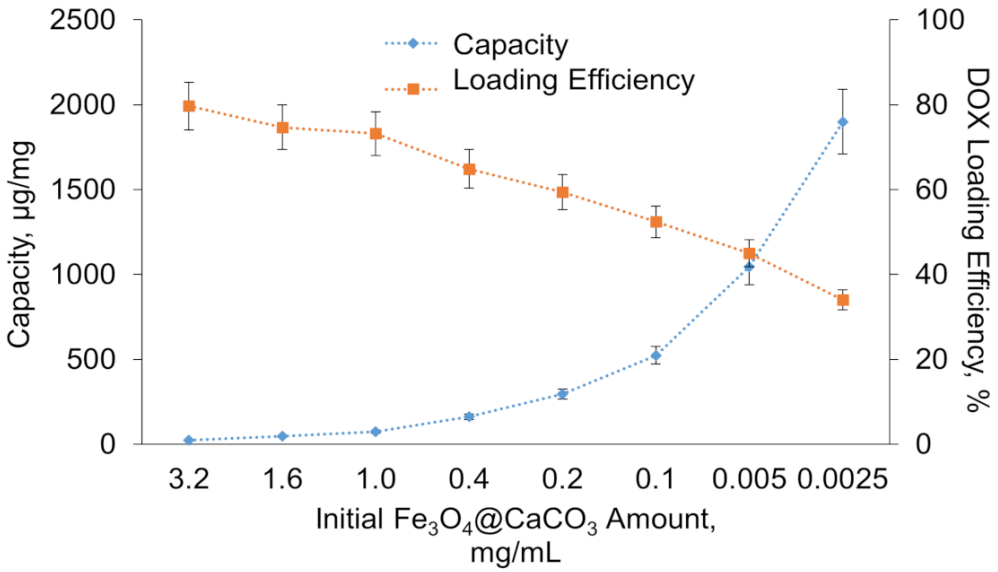

Figure 5. Dependence of Fe_3O_4@$CaCO_3$ capacity (μg/mg) and DOX loading efficiency (%) on nanoparticle concentration.

The initial Fe_3O_4@$CaCO_3$ and Fe_3O_4@$CaCO_3$/DOX samples with a capacity between 25 and 1045 μg/mg have a similar hydrodynamic diameter and ζ-potential (Table 2). The slight decrease in particle size with capacity increase perhaps occurs due to the increase in the packing density of DOX, which may be confirmed by changes in the nanoparticle density measured by TEM (Figure 6). The changes in ζ-potential and particle size in Fe_3O_4@$CaCO_3$/DOX with a high capacity of 1900 μg/mg are probably associated with a change in the predominant interactions from nanoparticle-DOX type (electrostatic interactions) to DOX-DOX type (hydrophobic interactions) (Figure S4). Furthermore, according to Figure 5, the capacity and efficacy curves intersect at a point of 1045 μg/mg. Such a capacity is considered optimal in terms of drug consumption. However, the difference in intermolecular interactions may lead to changes in drug pH-sensitive release efficiency, which is investigated in Section 3.3.

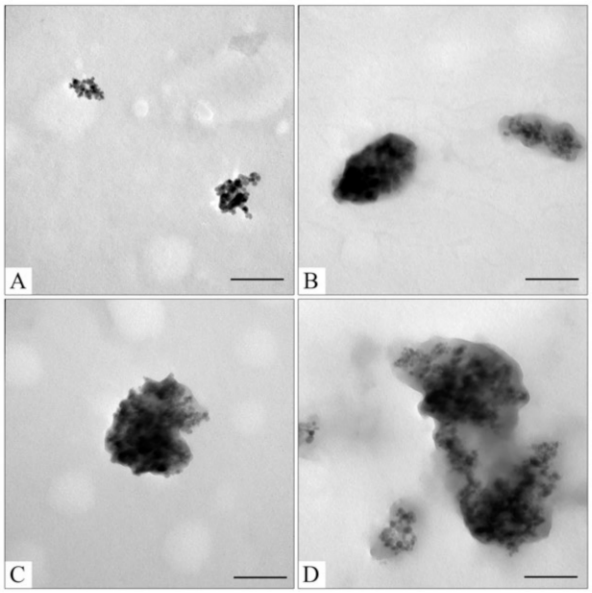

Figure 6. TEM images of Fe_3O_4@$CaCO_3$/DOX73 (**A**); Fe_3O_4@$CaCO_3$/DOX295 (**B**); Fe_3O_4@$CaCO_3$/DOX525 (**C**); Fe_3O_4@$CaCO_3$/DOX1045 (**D**). The bar indicates 100 nm.

3.3. Doxorubicin Release

The pH-sensitive DOX release efficiency is an essential factor. The release of DOX from various Fe_3O_4@$CaCO_3$/DOX nanocomposites was investigated at pH 4.0, 5.0, 6.0, and 7.4 (Table 3, Figure 7 and Figure S5). The pH range was selected from plasma pH of 7.4 to acidic, mimicking tumor microenvironment and cell endosomes (pH~5). The concentration of the released DOX was measured spectrophotometrically and using fluorescence with a Clariostar plate reader (BMG Labtech, Ortenberg, Germany). The nanocomposites showed pH-dependent drug distribution. Nanocomposites are presented in Table 3 and Figure 7, with their capacity decrypted at the end of the abbreviation. For example, Fe_3O_4@$CaCO_3$/DOX25 means DOX-loaded Fe_3O_4@$CaCO_3$ nanocomposite with 25 µg/mg DOX capacity. We calculated the DOX release efficiency as a percent of the initial DOX amount and in absolute values (µg/mL). As expected, DOX release was more efficient in acidic pH, which is in good correlation with previously published works [41,72]. Figure 7B and Table 3 indicate that the nanocomposites Fe_3O_4@$CaCO_3$/DOX25-45 are characterized by a 100% release of the drug at pH 5.0. The increase in nanoparticle capacity results in a lower release efficiency of up to 44–70% (Fe_3O_4@$CaCO_3$/DOX73–295) and 21–23% (Fe_3O_4@$CaCO_3$/DOX525–1900).

Table 3. DOX release efficiency from Fe_3O_4@$CaCO_3$/DOX at pH 4.0–7.4 at 25 °C for 24 h.

Sample Abbreviation with Capacity	pH 4.0		pH 5.0		pH 6.0		pH 7.4	
	C DOX, %	C DOX, µg/mL	C DOX, %	C DOX, µg/mL	C DOX, %	C DOX, µg/mL	C DOX, %	C DOX, µg/mL
Fe_3O_4@$CaCO_3$/DOX25	98 ± 4	2.4 ± 0.1	99 ± 1	2.48 ± 0.03	68 ± 3	1.69 ± 0.05	60 ± 4	1.5 ± 0.1
Fe_3O_4@$CaCO_3$/DOX45	94 ± 6	4.2 ± 0.3	98 ± 2	4.41 ± 0.09	49 ± 4	2.2 ± 0.2	57 ± 4	2.6 ± 0.1
Fe_3O_4@$CaCO_3$/DOX73	71 ± 5	5.2 ± 0.4	65 ± 4	4.8 ± 0.3	38 ± 1	2.8 ± 0.1	37 ± 4	2.7 ± 0.1
Fe_3O_4@$CaCO_3$/DOX160	65 ± 6	10 ± 1	59 ± 5	9.4 ± 0.8	26 ± 2	4.2 ± 0.3	21 ± 2	3.4 ± 0.1
Fe_3O_4@$CaCO_3$DOX295	44 ± 4	13 ± 1	32 ± 3	9.4 ± 0.9	17 ± 1	5.0 ± 0.3	12 ± 2	3.5 ± 0.1
Fe_3O_4@$CaCO_3$/DOX525	23 ± 2	12 ± 1	25 ± 2	13 ± 1	11.4 ± 0.4	6.0 ± 0.2	9 ± 3	4.7 ± 0.2
Fe_3O_4@$CaCO_3$/DOX1045	23 ± 2	24 ± 2	25 ± 3	26 ± 3	11.1 ± 0.8	12.1 ± 0.8	7 ± 2	7.3 ± 0.2
Fe_3O_4@$CaCO_3$/DOX1900	21 ± 2	44 ± 4	17 ± 1	32 ± 2	6.8 ± 0.5	13 ± 1	4 ± 1	7.6 ± 0.3

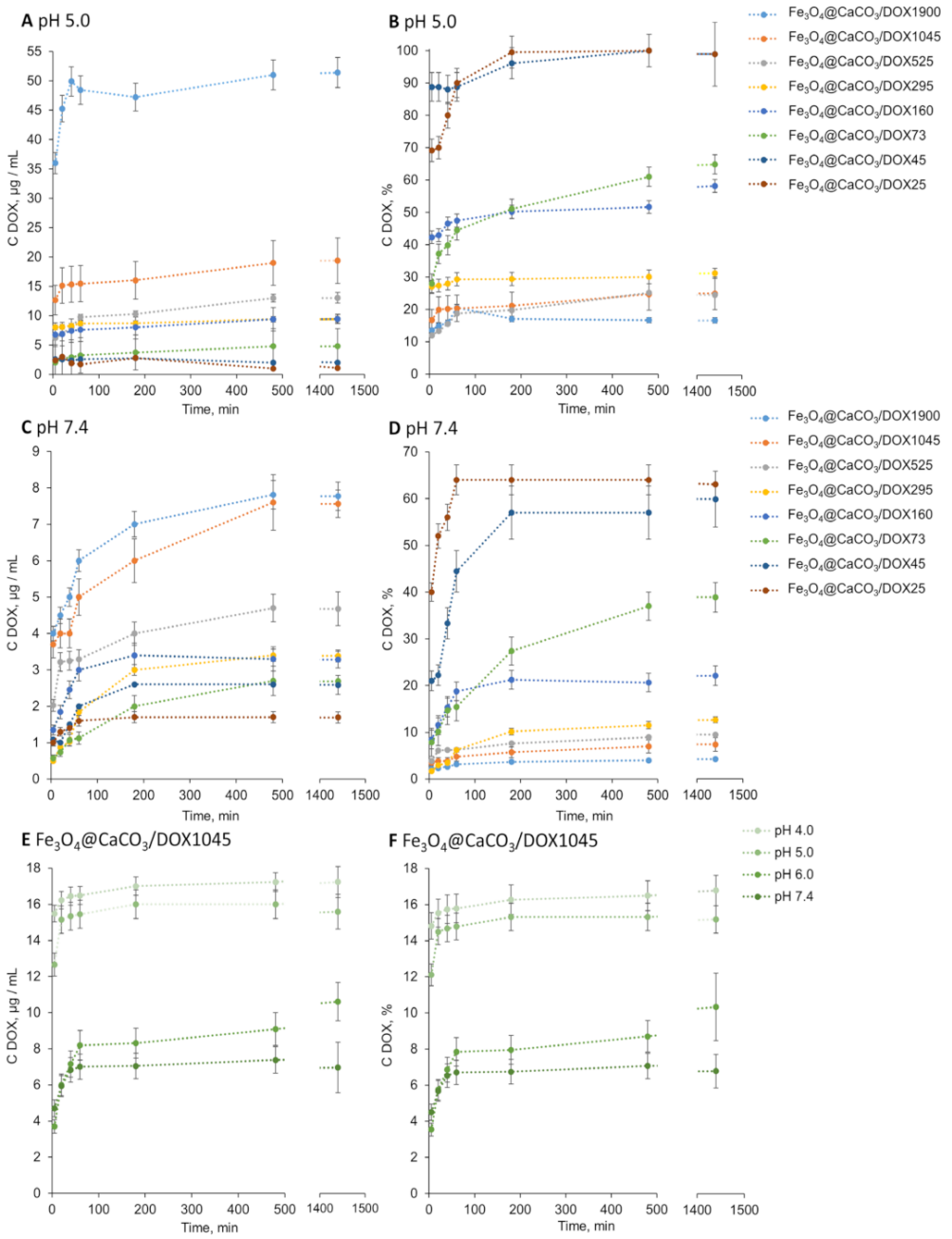

Figure 7. DOX release from Fe_3O_4@$CaCO_3$/DOX with capacity from 25 to 1900 μg/mg at pH 5.0 (**A**,**B**) and pH 7.4 (**C**,**D**) at 25 °C. DOX release from Fe_3O_4@$CaCO_3$/DOX with capacity 1045 μg/mg at pH 4.0–7.4 at 25 °C (**E**,**F**).

There is a tendency for decrease in release percentage with increasing nanocomposite capacity over the entire pH range studied (Figure 7, Table 3). However, the recalculation to the absolute values (μg/mL, Figure 6A) leads to a clear demonstration of Fe_3O_4@$CaCO_3$/DOX1900 and Fe_3O_4@$CaCO_3$/DOX1045 nanocomposites' achievements. Fe_3O_4@$CaCO_3$/DOX1900 is 2.7 times more effective than Fe_3O_4@$CaCO_3$/DOX1045 and 5.4 times more effective than Fe_3O_4@$CaCO_3$/DOX160 at pH 5.0 (Figure 6A). Moreover, the most efficient nanocomposite at pH 4-5, Fe_3O_4@$CaCO_3$/DOX1900 showed seven times less DOX release in the physiological pH region, which is 4% of the total amount of the loaded drug. These indicators are promising for further studies of nanoparticles as a container for anticancer drugs. Moreover, at this stage, particles with a capacity of 1900 μg/mL can

be distinguished from the obtained nanocomposites as the most effective in terms of the absolute values (μg/mL) of the released drug.

3.4. Cellular Toxicity Study of Fe_3O_4@$CaCO_3$ and Fe_3O_4@$CaCO_3$/DOX

The cytotoxicity of Fe_3O_4@$CaCO_3$ and Fe_3O_4@$CaCO_3$/DOX nanocomposites was studied on HeLa (cervical cancer) and MCF-7 (breast cancer) cell lines. Fe_3O_4@$CaCO_3$ showed extremely low cytotoxicity in the wide concentration range of up to 2 mg/mL (Figure 8). $CaCO_3$ is endowed with high biocompatibility and the absence of hemolytic effect, which was shown by a number of works [39–44,90]. Several works show the safety of nanoscale Fe_3O_4@$CaCO_3$ of up to 0.8 mg/mL [47].

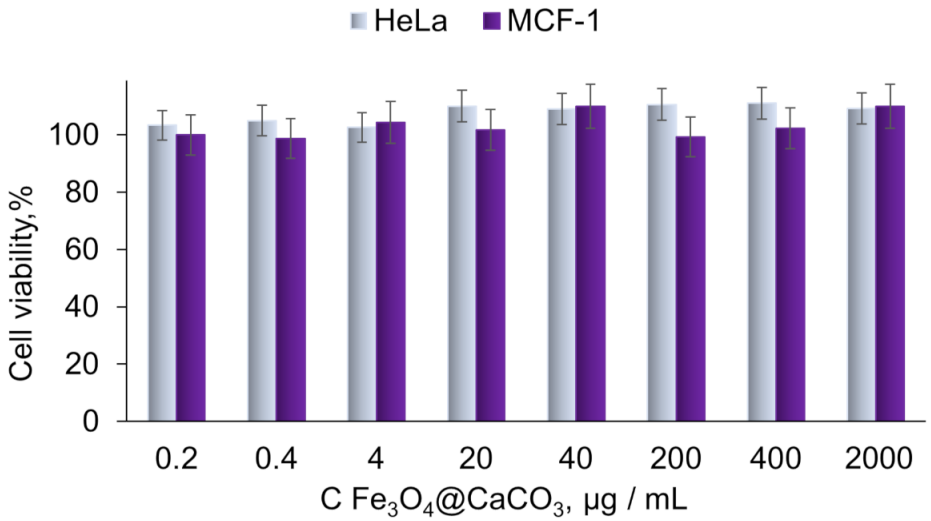

Figure 8. Cell viability assay using MTT. HeLa and MCF-7 cells were incubated with Fe_3O_4@$CaCO_3$ for 48 h.

Fe_3O_4@$CaCO_3$/DOX nanocomposites and DOX cell viability experiments were performed at the same DOX concentration (μM) in cell media or the concentration of nanoparticles (μg/mL) (Figure 9). Fe_3O_4@$CaCO_3$/DOX25-1900 nanocomposites effectively suppressed cellular activity. The experiment with the same concentration of DOX in the cell media showed comparable cell inhibition for DOX-loaded nanoparticles and free drug (Figure 9, left). However, Fe_3O_4@$CaCO_3$/DOX1900 indicated higher cell viability, which may be explained by prolonged drug release. Such an effect appears to a lesser degree for other DOX-loaded nanocomposites with a high capacity (Figure 9, left). This fact confirms the data on DOX release efficiency at physiological pH (Table 3, % columns). The diagram in Figure 9 on the right correlates with the release data in absolute values (Table 3, μg/mL columns). These data show the impressive potential of Fe_3O_4@$CaCO_3$/DOX with a capacity higher than 160 μg/mg. Of course, more pronounced cell inhibition was found for 1045 and 1900 μg/mg capacity.

The half-maximum inhibitory concentration (IC 50) (Table 4) in terms of Fe_3O_4@$CaCO_3$/DOX concentration (μg/mL) looks consistent and confirms all previously obtained results as well as the persistence of the inhibitory activity of DOX in the nanocomposite. When normalizing the results of the MTT test to the DOX concentration, we observed the best IC 50 in particles with a higher release efficiency in percent (Fe_3O_4@$CaCO_3$/DOX160), and when normalizing to the concentration of nanoparticles, the best IC 50 in particles with the maximum loading capacity (Fe_3O_4@$CaCO_3$/DOX1900). The presented work is the first one describing Fe_3O_4@$CaCO_3$/DOX nanocomposites. When comparing Fe_3O_4@$CaCO_3$/DOX with nanoscale Fe_3O_4/DOX and $CaCO_3$/DOX, it can be seen that the developed system is more effective [41,72,91–93].

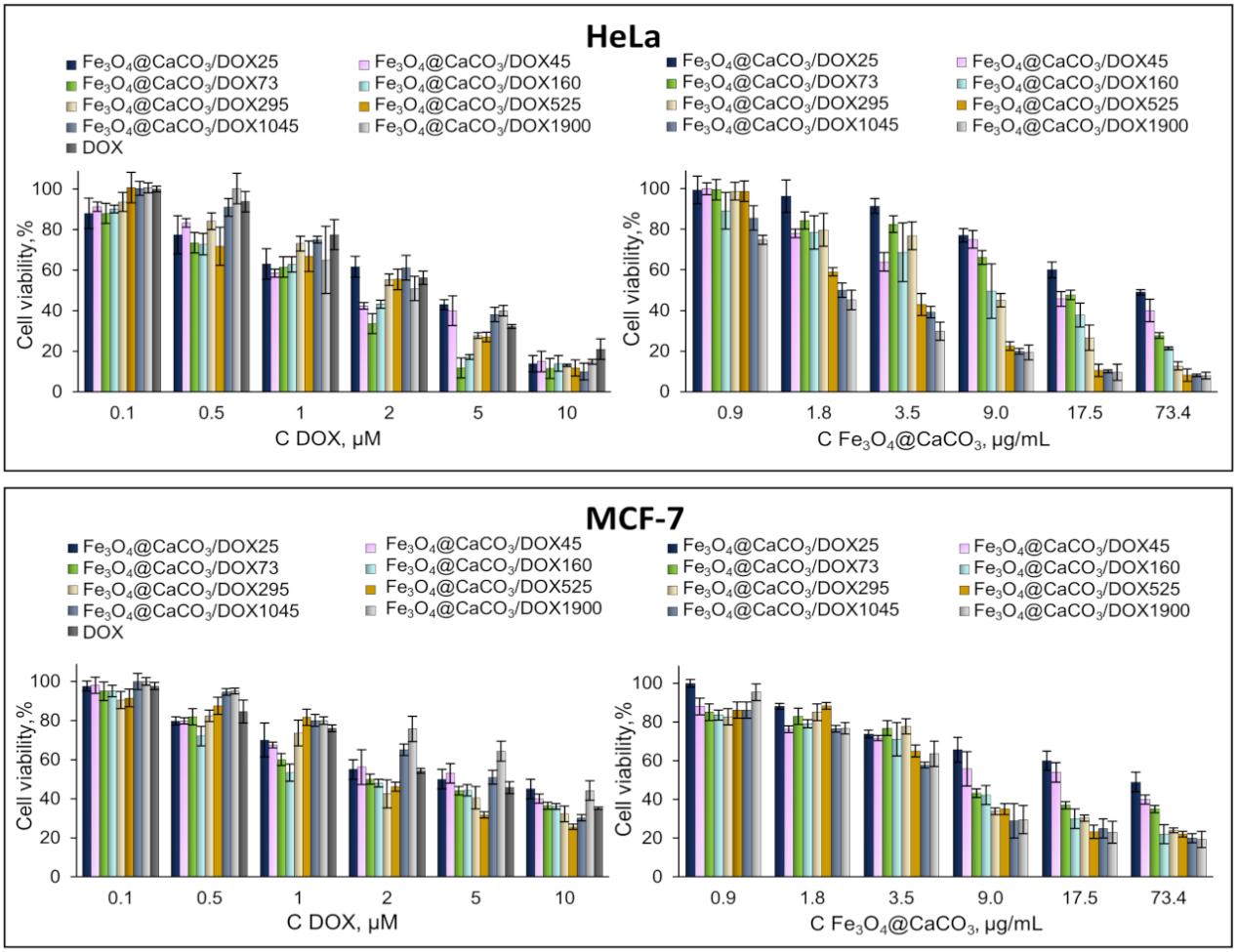

Figure 9. Cell viability assay using MTT. HeLa and MCF-7 cells were incubated with Fe_3O_4@$CaCO_3$/DOX and free DOX for 48 h.

Table 4. IC 50 of different types of Fe_3O_4@$CaCO_3$/DOX and free DOX on HeLa and MCF-7 cells.

Sample	HeLa		MCF-7	
	IC 50, μM DOX	**IC 50, μg/mL Fe_3O_4@$CaCO_3$/DOX**	**IC 50, μM DOX**	**IC 50, μg/mL Fe_3O_4@$CaCO_3$/DOX**
Fe_3O_4@$CaCO_3$/DOX25	3.0	49.5	5.2	60.0
Fe_3O_4@$CaCO_3$/DOX45	1.8	22.0	4.5	41.6
Fe_3O_4@$CaCO_3$/DOX73	1.6	13.8	2.5	16.4
Fe_3O_4@$CaCO_3$/DOX160	**1.2**	7.0	**2.0**	9.9
Fe_3O_4@$CaCO_3$/DOX295	2.3	5.8	2.2	7.6
Fe_3O_4@$CaCO_3$/DOX525	2.4	2.4	3.1	4.3
Fe_3O_4@$CaCO_3$/DOX1045	2.5	1.9	5.2	4.1
Fe_3O_4@$CaCO_3$/DOX1900	2.6	**1.5**	5.7	**3.5**
DOX	2.8	—	3.1	—

3.5. Human Serum Albumin Interaction with Fe_3O_4@$CaCO_3$/DOX

On entering biological fluids, the surface of the nanomaterials is quickly coated with biomolecules forming a bioinspired coating [94]. Serum or cellular proteins can form strongly and weakly adsorbed protein coating, known as "hard and soft nanoparticle corona," respectively [94]. For instance, the protein corona produces stealth-like properties, improving biodistribution, biocompatibility, cellular interaction, and the recognition

of nanoparticles by immune cells [95–98]. The adsorbed protein may conceal targeting molecules on the nanoparticle surface and dictate the bio-reactivity [98]. In human plasma, a typical nanoparticle corona consists of major proteins such as serum albumin, immunoglobulins, fibrinogen, apolipoproteins, etc. [98,99]. Overall, the most abundant corona protein is serum albumin, which arranges a "crash test" for drugs and nanoparticles [99].

Human serum albumin (HSA) is a major transport human plasma protein. It is important for organism functions and forms covalent and reversible dimers, oligomers, and posttranslational modifications [3,100]. Various albumin-based multifunctional constructions were synthesized for therapy and diagnostic applications [3,101–105]. HSA influences drug pharmacokinetics and pharmacodynamics. Nanomaterials getting into the blood interact with albumin forming a corona on the surface, which highly changes stability, biodistribution, and pharmacokinetics, and reduces the hemolytic effect on red blood cells and toxicity [3,96,98,106–109]. Furthermore, albumin-coated nanoparticles demonstrated enhanced cell uptake and more efficient tumor targeting due to the EPR effect and interaction with receptors (e.g., gp60, SPARC, etc.) [3]. The next logical step would be the use of albumin corona as a stealth-coating material by fabricating protein-inorganic core nanocomposites in a controlled condition [96]. It is not only critical for "stealthily" properties but also shows the possible material stability or unexpected drug release in blood. The influence of HSA on Fe_3O_4@$CaCO_3$/DOX nanocomposites' stability was tested in 10 mM PBS (pH 7.4) at 37 °C for 12 h, modeling the condition in the human body (Table 5). The results indicate DOX release and HSA binding to the nanocomposites. TEM images showed the destruction of the DOX film and the formation of a protein corona on the surface (cf. Figures 6C and 10). Higher physiological albumin concentration (32 mg/mL, 0.48 mM) leads to higher drug release. For the different Fe_3O_4@$CaCO_3$/DOX, HSA loading efficiency is the same indicating the saturation of the nanocomposites' surface binding with protein. However, Fe_3O_4@$CaCO_3$/DOX loses only a small amount of drug, keeping the retained DOX in the nanocomposite (Table 5).

Table 5. HSA loading on Fe_3O_4@$CaCO_3$/DOX nanocomposites.

Sample	Initial C HSA mg/mL	Remaining C DOX, %	DOX capacity in Fe_3O_4@$CaCO_3$ after Incubation, μg/mg	HSA Loading Efficiency, %
Fe_3O_4@$CaCO_3$/DOX160	3.2	20 ± 2	32 ± 3	16 ± 1
	32	6 ± 1	10 ± 2	18 ± 2
Fe_3O_4@$CaCO_3$/DOX525	3.2	65 ± 2	341 ± 10	13 ± 1
	32	60 ± 3	315 ± 16	16 ± 1
Fe_3O_4@$CaCO_3$/DOX1900	3.2	71 ± 2	1539 ± 45	12.3 ± 0.7
	32	64 ± 1	1215 ± 19	18.5 ± 0.5

Afterward, the samples were separated and used for the MTT test (Figure 10), which is usually used for primary toxicity studies. However, the MTT assay does not show non-specific interaction with blood and tissue, or chronic toxicity. Compared to Fe_3O_4@$CaCO_3$/DOX, the albumin-substituted nanocomposites provide much higher cell viability. We assumed that the albumin corona hides DOX molecules, thereby inhibiting acute toxicity. Nevertheless, the therapeutic effect is retained, which may be revealed in cancer tissue (Figure 11). The preformed albumin corona prevents possible non-specific drug release in human plasma, leading to organism-friendly, less toxic nanoplatform. The interaction between nanocomposite and albumin may also reduce systemic toxicity. However, the presented results require further investigation.

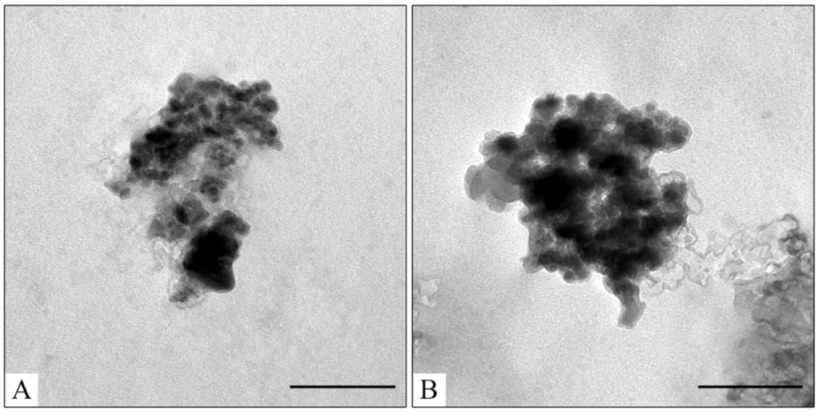

Figure 10. TEM images of Fe_3O_4@$CaCO_3$/DOX525-HSA3.2 (**A**) and Fe_3O_4@$CaCO_3$/DOX525-HSA32 (**B**). The bar indicates 100 nm.

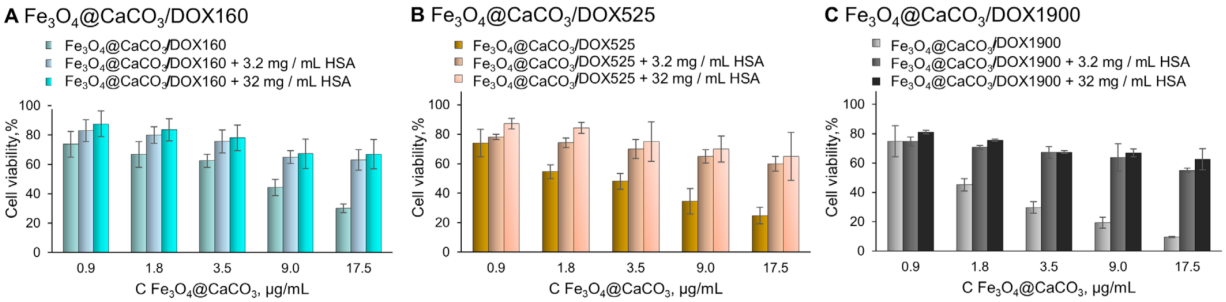

Figure 11. Cell viability assay using MTT. MCF-7 cells were incubated with Fe_3O_4@$CaCO_3$/DOX and Fe_3O_4@$CaCO_3$/DOX-HSA for 48 h.

4. Conclusions

In summary, magnetic Fe_3O_4@$CaCO_3$ nanocomposites were obtained using the co-precipitation method, yielding a porous superstructure over the magnetic core. TEM and DLS methods demonstrated that the obtained Fe_3O_4@$CaCO_3$ MNCs were 135 nm in size and possessed narrow size distributions. The resultant MNCs showed high stability in the physiological conditions, slightly acidic pH, cell media, and FBS. The material showed low cytotoxicity and high biocompatibility. We investigated the possible drug doxorubicin (DOX) loading set up using a series of experiments. This method provided a high DOX capacity of up to 1900 μg/mg (DOX/MNPs) with a pH-responsible drug release. The remaining DOX-loaded MNCs were stable in neutral pH and enabled drug extrication in a mild pH medium with high efficiency. The acidic pH mimics the cancer tumor environment and cell organelle media. Due to the suitable size, magnetic properties, and high drug loading capacity, Fe_3O_4@$CaCO_3$/DOX is suitable for further in vivo experiments. The series of DOX-loaded Fe3O4@CaCO3 MNCs indicated an excellent inhibition of Hela and MCF-7 cell lines, and the IC 50 values were calculated. The cell viability studies of the series of Fe_3O_4@$CaCO_3$/DOX MNCs with different drug capacities showed the optimal drug loading of 160 μg/mg per DOX concentration and 1900 μg/mg per nanoparticles amount. However, the higher loading of 1900 μg/mg is the perspective for prolonged clinical effects using low-dose MNCs. The IC 50 values (HeLa cells) were calculated as 2.6 μM in terms of DOX and 1.5 μg/mL in terms of the nanoparticles' amount. The stability experiments for DOX-loaded Fe_3O_4@$CaCO_3$ in HSA solution indicated the drug release due to the formation of a protein corona. An experiment should be conducted for any composites that will interact with HSA and other plasma proteins. We assumed that HSA pushed out the DOX molecules, interacting with the MNCs' surface with a certain capacity. Afterward, the sorption was disrupted, yielding a stable construction, which will not release DOX easily in plasma media. Moreover, the new layer of albumin super coating may increase tumor

capture of drug-loaded MNCs. HSA coating increases the colloidal stability, prolongs blood circulation time, and prevents non-specific adsorption of blood components. HSA increases the efficiency of tissue and cell targeting due to the EPR effect and receptor interaction. Finally, DOX-loaded MNCs may offer a high potential for pH-sensitive nanotheranostic areas for drug-resistance cancer treatment.

To sum up, the proposed excellent, biocompatible Fe_3O_4@$CaCO_3$ nanocomposite is a good platform for drug delivery and disease treatment. Despite the promising results in the synthesis, drug-loading, and release of Fe_3O_4@$CaCO_3$, numerous challenges must be addressed for cancer treatment. The optimization of the structure concerning magnetic resonance imaging or hyperthermia properties targeted magnetic transport, and address molecule modification should be carried out. Extensive in vitro or cell experiments should be conducted, involving toxicity, targeting efficacy, and biocompatibility. After these important stages, the functional nanoplatform may be applied to in vivo studies for clinical prospects evaluation. Meanwhile, the Fe_3O_4@$CaCO_3$ nanoplatform may be considered for various applications of MNCs [35].

Supplementary Materials: The following supporting information can be downloaded at: https://www.mdpi.com/article/10.3390/pharmaceutics15030771/s1, Figure S1: DLS size distribution of Fe_3O_4@$CaCO_3$ (0.45 mg/mL of Fe_3O_4 synthesis) by number (top), volume (middle) and intensity (bottom) obtained by adding 0.45 mg/mL; Figure S2: DLS size distribution of Fe_3O_4@$CaCO_3$ by number (top), volume (middle), intensity (bottom) after 5 months of storage at 7 °C in deionized water. The particle size was determined using DLS (139 ± 5 nm, PDI of 0.33 ± 0.01); Figure S3: The hydrodynamic diameter by DLS of Fe_3O_4@$CaCO_3$ in various solutions; Figure S4: Possible nanoparticle interactions with doxorubicin (DOX); Figure S5: The proportion of DOX release from Fe_3O_4@$CaCO_3$/DOX (capacity, 25–1900 μg/mg) at pH 4.0 (A, C); pH 6.0 (B, D); Figure S6: The confirmation of DOX-loading using photography. The left photograph also shows magnetic behavior on the magnetic tube rack; Figure S7: Fluorescence and UV-vis spectra of Fe3O4@CaCO3/DOX nanocomposites.

Author Contributions: Senior researchers A.C. and E.D. contributed equally to the work and share senior authorship. Conceptualization, A.C. and E.D.; methodology, A.C. and E.D.; investigation, V.P. and Y.P.; data curation, V.P. and Y.P.; writing—original draft preparation, A.C., V.P. and E.D.; project administration, A.C. and E.D.; funding acquisition, A.C. and E.D. All authors have read and agreed to the published version of the manuscript.

Funding: This study was funded by the Russian Science Foundation (grant no. 21-74-00120), and the cell experiments were partially funded by the Ministry of Science and Higher Education of the Russian Federation (state registration no. 121031300042-1).

Institutional Review Board Statement: Not applicable.

Informed Consent Statement: Not applicable.

Data Availability Statement: The data are contained in the article.

Acknowledgments: The author thanks the technician of ICBFM SB RAS Grigorieva E. for cell room and cell cultures maintenance work. Authors would like to acknowledge the Multi-Access Chemical Research Center of N.N. Vorozhtsov Novosibirsk Institute of Organic Chemistry SB RAS for FTIR spectra recording.

Conflicts of Interest: The authors declare no conflict of interest. The funders had no role in the design of the study; in the collection, analyses, or interpretation of data; in the writing of the manuscript; or in the decision to publish the results.

References

1. Popova, V.; Dmitrienko, E.; Chubarov, A. Magnetic Nanocomposites and Imprinted Polymers for Biomedical Applications of Nucleic Acids. *Magnetochemistry* **2023**, *9*, 12. [CrossRef]
2. Petrov, K.D.; Chubarov, A.S. Magnetite Nanoparticles for Biomedical Applications. *Encyclopedia* **2022**, *2*, 1811–1828. [CrossRef]
3. Chubarov, A.S. Serum Albumin for Magnetic Nanoparticles Coating. *Magnetochemistry* **2022**, *8*, 13. [CrossRef]

4. Anderson, S.D.; Gwenin, V.V.; Gwenin, C.D. Magnetic Functionalized Nanoparticles for Biomedical, Drug Delivery and Imaging Applications. *Nanoscale Res. Lett.* **2019**, *14*, 1–16. [CrossRef] [PubMed]
5. Lamichhane, N.; Sharma, S.; Parul; Verma, A.K.; Roy, I.; Sen, T. Iron Oxide-Based Magneto-Optical Nanocomposites for in Vivo Biomedical Applications. *Biomedicines* **2021**, *9*, 288. [CrossRef] [PubMed]
6. Creţu, B.E.B.; Dodi, G.; Shavandi, A.; Gardikiotis, I.; Şerban, I.L.; Balan, V. Imaging Constructs: The Rise of Iron Oxide Nanoparticles. *Molecules* **2021**, *26*, 3437. [CrossRef] [PubMed]
7. Anik, M.I.; Hossain, M.K.; Hossain, I.; Mahfuz, A.M.U.B.; Rahman, M.T.; Ahmed, I. Recent Progress of Magnetic Nanoparticles in Biomedical Applications: A Review. *Nano Sel.* **2021**, *2*, 1146–1186. [CrossRef]
8. Mittal, A.; Gandhi, S.; Roy, I. Mechanistic Interaction Studies of Synthesized ZIF-8 Nanoparticles with Bovine Serum Albumin Using Spectroscopic and Molecular Docking Approaches. *Sci. Rep.* **2022**, *12*, 10331. [CrossRef]
9. Comanescu, C. Magnetic Nanoparticles: Current Advances in Nanomedicine, Drug Delivery and MRI. *Chemistry* **2022**, *4*, 872–930. [CrossRef]
10. Włodarczyk, A.; Gorgoń, S.; Radoń, A.; Bajdak-Rusinek, K. Magnetite Nanoparticles in Magnetic Hyperthermia and Cancer Therapies: Challenges and Perspectives. *Nanomaterials* **2022**, *12*, 1807. [CrossRef]
11. Materón, E.M.; Miyazaki, C.M.; Carr, O.; Joshi, N.; Picciani, P.H.S.; Dalmaschio, C.J.; Davis, F.; Shimizu, F.M. Magnetic Nanoparticles in Biomedical Applications: A Review. *Appl. Surf. Sci. Adv.* **2021**, *6*, 100163. [CrossRef]
12. Mittal, A.; Roy, I.; Gandhi, S. Magnetic Nanoparticles: An Overview for Biomedical Applications. *Magnetochemistry* **2022**, *8*, 107. [CrossRef]
13. Krishnan, S.; Goud, K.Y. Magnetic Particle Bioconjugates: A Versatile Sensor Approach. *Magnetochemistry* **2019**, *5*, 64. [CrossRef]
14. Frenea-Robin, M.; Marchalot, J. Basic Principles and Recent Advances in Magnetic Cell Separation. *Magnetochemistry* **2022**, *8*, 11. [CrossRef]
15. Mariño, M.A.; Fulaz, S.; Tasic, L. Magnetic Nanomaterials as Biocatalyst Carriers for Biomass Processing: Immobilization Strategies, Reusability, and Applications. *Magnetochemistry* **2021**, *7*, 133. [CrossRef]
16. Chouhan, R.S.; Horvat, M.; Ahmed, J.; Alhokbany, N.; Alshehri, S.M.; Gandhi, S. Magnetic Nanoparticles—A Multifunctional Potential Agent for Diagnosis and Therapy. *Cancers* **2021**, *13*, 2213. [CrossRef] [PubMed]
17. Bobrikova, E.; Chubarov, A.; Dmitrienko, E. The Effect of PH and Buffer on Oligonucleotide Affinity for Iron Oxide Nanoparticles. *Magnetochemistry* **2021**, *7*, 128. [CrossRef]
18. Bulgakova, A.; Chubarov, A.; Dmitrienko, E. Magnetic Nylon 6 Nanocomposites for the Microextraction of Nucleic Acids from Biological Samples. *Magnetochemistry* **2022**, *8*, 85. [CrossRef]
19. Zhong, Y.; Chen, C.; Liu, S.; Lu, C.; Liu, D.; Pan, Y.; Sakiyama, H.; Muddassir, M.; Liu, J. A New Magnetic Adsorbent of Eggshell-Zeolitic Imidazolate Framework for Highly Efficient Removal of Norfloxacin. *Dalt. Trans.* **2021**, *50*, 18016–18026. [CrossRef]
20. Zheng, R.; Guo, J.; Cai, X.; Bin, L.; Lu, C.; Singh, A.; Trivedi, M.; Kumar, A.; Liu, J. Manganese Complexes and Manganese-Based Metal-Organic Frameworks as Contrast Agents in MRI and Chemotherapeutics Agents: Applications and Prospects. *Colloids Surf. B Biointerfaces* **2022**, *213*, 112432. [CrossRef]
21. Li, C.; Chen, T.; Ocsoy, I.; Zhu, G.; Yasun, E.; You, M.; Wu, C.; Zheng, J.; Song, E.; Huang, C.Z.; et al. Gold-Coated Fe_3O_4 Nanoroses with Five Unique Functions for Cancer Cell Targeting, Imaging, and Therapy. *Adv. Funct. Mater.* **2014**, *24*, 1772–1780. [CrossRef]
22. Shen, S.; Wu, L.; Liu, J.; Xie, M.; Shen, H.; Qi, X.; Yan, Y.; Ge, Y.; Jin, Y. Core-Shell Structured Fe_3O_4@TiO_2-Doxorubicin Nanoparticles for Targeted Chemo-Sonodynamic Therapy of Cancer. *Int. J. Pharm.* **2015**, *486*, 380–388. [CrossRef]
23. Shabatina, T.I.; Vernaya, O.I.; Shabatin, V.P.; Melnikov, M.Y. Magnetic Nanoparticles for Biomedical Purposes: Modern Trends and Prospects. *Magnetochemistry* **2020**, *6*, 30. [CrossRef]
24. Ganapathe, L.S.; Mohamed, M.A.; Yunus, R.M.; Berhanuddin, D.D. Magnetite (Fe_3O_4) Nanoparticles in Biomedical Application: From Synthesis to Surface Functionalisation. *Magnetochemistry* **2020**, *6*, 68. [CrossRef]
25. Hepel, M. Magnetic Nanoparticles for Nanomedicine. *Magnetochemistry* **2020**, *6*, 3. [CrossRef]
26. Dulińska-Litewka, J.; Łazarczyk, A.; Hałubiec, P.; Szafrański, O.; Karnas, K.; Karewicz, A. Superparamagnetic Iron Oxide Nanoparticles-Current and Prospective Medical Applications. *Materials* **2019**, *12*, 617. [CrossRef] [PubMed]
27. Stueber, D.D.; Villanova, J.; Aponte, I.; Xiao, Z. Magnetic Nanoparticles in Biology and Medicine: Past, Present, and Future Trends. *Pharmaceutics* **2021**, *13*, 943. [CrossRef] [PubMed]
28. Socoliuc, V.; Peddis, D.; Petrenko, V.I.; Avdeev, M.V.; Susan-Resiga, D.; Szabó, T.; Turcu, R.; Tombácz, E.; Vékás, L. Magnetic Nanoparticle Systems for Nanomedicine—A Materials Science Perspective. *Magnetochemistry* **2020**, *6*, 2. [CrossRef]
29. Bruschi, M.L.; de Toledo, L.D.A.S. Pharmaceutical Applications of Iron-Oxide Magnetic Nanoparticles. *Magnetochemistry* **2019**, *5*, 50. [CrossRef]
30. Ajalli, N.; Pourmadadi, M.; Yazdian, F.; Rashedi, H.; Navaei-Nigjeh, M.; Díez-Pascual, A.M. Chitosan/Gamma-Alumina/Fe_3O_4@5-FU Nanostructures as Promising Nanocarriers: Physiochemical Characterization and Toxicity Activity. *Molecules* **2022**, *27*, 5369. [CrossRef]
31. Schubert, J.; Chanana, M. Coating Matters: Review on Colloidal Stability of Nanoparticles with Biocompatible Coatings in Biological Media, Living Cells and Organisms. *Curr. Med. Chem.* **2018**, *25*, 4553–4586. [CrossRef] [PubMed]
32. Issa, B.; Obaidat, I.M.; Albiss, B.A.; Haik, Y. Magnetic Nanoparticles: Surface Effects and Properties Related to Biomedicine Applications. *Int. J. Mol. Sci.* **2013**, *14*, 21266–21305. [CrossRef]

33. Kudr, J.; Haddad, Y.; Richtera, L.; Heger, Z.; Cernak, M.; Adam, V.; Zitka, O. Magnetic Nanoparticles: From Design and Synthesis to Real World Applications. *Nanomaterials* **2017**, *7*, 243. [CrossRef]
34. Schwaminger, S.P.; Bauer, D.; Fraga-García, P. Gold-Iron Oxide Nanohybrids: Insights into Colloidal Stability and Surface-Enhanced Raman Detection. *Nanoscale Adv.* **2021**, *3*, 6438–6445. [CrossRef] [PubMed]
35. Mourdikoudis, S.; Kostopoulou, A.; LaGrow, A.P. Magnetic Nanoparticle Composites: Synergistic Effects and Applications. *Adv. Sci.* **2021**, *8*, 2004951. [CrossRef]
36. Zou, H.; Luo, Z.; Yang, X.; Xie, Q.; Zhou, Y. Toward Emerging Applications Using Core–Shell Nanostructured Materials: A Review. *J. Mater. Sci.* **2022**, *57*, 10912–10942. [CrossRef]
37. Dinc, M.; Esen, C.; Mizaikoff, B. Recent Advances on Core–Shell Magnetic Molecularly Imprinted Polymers for Biomacromolecules. *Trends Anal. Chem.* **2019**, *114*, 202–217. [CrossRef]
38. Gopalan Sibi, M.; Verma, D.; Kim, J. Magnetic Core–Shell Nanocatalysts: Promising Versatile Catalysts for Organic and Photocatalytic Reactions. *Catal. Rev. Sci. Eng.* **2020**, *62*, 163–311. [CrossRef]
39. Trofimov, A.D.; Ivanova, A.A.; Zyuzin, M.V.; Timin, A.S. Porous Inorganic Carriers Based on Silica, Calcium Carbonate and Calcium Phosphate for Controlled/Modulated Drug Delivery: Fresh Outlook and Future Perspectives. *Pharmaceutics* **2018**, *10*, 167. [CrossRef]
40. Zhao, P.; Tian, Y.; You, J.; Hu, X. Recent Advances of Calcium Carbonate Nanoparticles for Biomedical Applications. *Bioengineering* **2022**, *9*, 691. [CrossRef]
41. Popova, V.; Poletaeva, Y.; Pyshnaya, I.; Pyshnyi, D.; Dmitrienko, E. Designing PH-Dependent Systems Based on Nanoscale Calcium Carbonate for the Delivery of an Antitumor Drug. *Nanomaterials* **2021**, *11*, 2794. [CrossRef] [PubMed]
42. Luo, W.; Hua, J.; Xie, X. Polyethylenimine-CO2 Adduct-Stabilized Vaterite Hydrocolloidal Particles. *Mater. Chem. Phys.* **2023**, *294*, 127025. [CrossRef]
43. Persano, F.; Nobile, C.; Piccirillo, C.; Gigli, G.; Leporatti, S. Monodisperse and Nanometric-Sized Calcium Carbonate Particles Synthesis Optimization. *Nanomaterials* **2022**, *12*, 1494. [CrossRef]
44. Atchudan, R.; Perumal, S.; Joo, J.; Lee, Y.R. Synthesis and Characterization of Monodispersed Spherical Calcium Oxide and Calcium Carbonate Nanoparticles via Simple Pyrolysis. *Nanomaterials* **2022**, *12*, 2424. [CrossRef] [PubMed]
45. Dong, Z.; Feng, L.; Zhu, W.; Sun, X.; Gao, M.; Zhao, H.; Chao, Y.; Liu, Z. $CaCO_3$ Nanoparticles as an Ultra-Sensitive Tumor-PH-Responsive Nanoplatform Enabling Real-Time Drug Release Monitoring and Cancer Combination Therapy. *Biomaterials* **2016**, *110*, 60–70. [CrossRef] [PubMed]
46. Zhang, W.; Li, Q.; Li, J.; Sun, X.; Shen, J.; Han, W.; Wang, L. The Preparation of Layered Hierarchical and Cube-Shaped Magnetic $Fe_3O_4/CaCO_3$ for Efficient Enrichment of Pb(II) from Aqueous Solutions. *Environ. Nanotechnol. Monit. Manag.* **2021**, *16*, 100600. [CrossRef]
47. Wang, P.; Xue, J.; Wu, S.; Pei, Y.; Xu, L.; Wang, Y. Cell-Friendly Isolation and PH-Sensitive Controllable Release of Circulating Tumor Cells by Fe_3O_4@$CaCO_3$ Nanoplatform. *Adv. Mater. Interfaces* **2021**, *8*, 2101191. [CrossRef]
48. Maleki Dizaj, S.; Sharifi, S.; Ahmadian, E.; Eftekhari, A.; Adibkia, K.; Lotfipour, F. An Update on Calcium Carbonate Nanoparticles as Cancer Drug/Gene Delivery System. *Expert Opin. Drug Deliv.* **2019**, *16*, 331–345. [CrossRef]
49. Vavaev, E.S.; Novoselova, M.; Shchelkunov, N.M.; German, S.; Aleksei, S.; Mokrousov, M.D.; Zelepukin, I.V.; Burov, A.M.; Khlebtsov, B.N.; Lyubin, E.V.; et al. $CaCO_3$ Nanoparticles Coated with Alternating Layers of Poly-L-Arginine Hydrochloride and Fe_3O_4 Nanoparticles as Navigable Drug Carriers and Hyperthermia Agents. *ACS Appl. Nano Mater.* **2022**, *5*, 2994–3006. [CrossRef]
50. Xue, J.; Li, X.; Li, Q.; Lyu, J.; Wang, W.; Zhuang, L.; Xu, Y. Magnetic Drug-Loaded Osteoinductive $Fe_3O_4/CaCO_3$ Hybrid Microspheres System: Efficient for Sustained Release of Antibiotics. *J. Phys. D Appl. Phys.* **2020**, *53*, 245401. [CrossRef]
51. Serov, N.; Prilepskii, A.; Sokolov, A.; Vinogradov, V. Synthesis of Plasmin-Loaded Fe_3O_4@$CaCO_3$ Nanoparticles: Towards Next-Generation Thrombolytic Drugs. *ChemNanoMat* **2019**, *5*, 1267–1271. [CrossRef]
52. Li, F.H.; Tang, N.; Wang, Y.Q.; Zhang, L.; Du, W.; Xiang, J.; Cheng, P.G. Synthesis and Characterization of Magnetic Carriers Based on Immobilized Enzyme. *IOP Conf. Ser. Mater. Sci. Eng.* **2018**, *359*, 012044. [CrossRef]
53. Lee, Y.H.; Seo, J.C.; Oh, Y.K.; Lee, K. Synthesis of Microaglae-Capturing Magnetic Microcapsule Using $CaCO_3$ Microparticles and Layer-by-Layer Coating. *Korean J. Mater. Res.* **2018**, *28*, 376–380. [CrossRef]
54. Han, P.; Jiang, Z.; Wang, X.; Wang, X.; Zhang, S.; Shi, J.; Wu, H. Facile Preparation of Porous Magnetic Polydopamine Microspheres through an Inverse Replication Strategy for Efficient Enzyme Immobilization. *J. Mater. Chem. B* **2015**, *3*, 7194–7202. [CrossRef]
55. Wang, C.; Yan, J.; Cui, X.; Cong, D.; Wang, H. Preparation and Characterization of Magnetic Hollow PMMA Nanospheres via in Situ Emulsion Polymerization. *Colloids Surf. A Physicochem. Eng. Asp.* **2010**, *363*, 71–77. [CrossRef]
56. Ma, H.; Zhou, J.; Caruntu, D.; Yu, M.H.; Chen, J.F.; O'Connor, C.J.; Zhou, W.L. Fabrication of Magnetic Porous Hollow Silica Drug Carriers Using $CaCO_3$ Fe_3O_4 Composite Nanoparticles and Cationic Surfactant Double Templates. *J. Appl. Phys.* **2008**, *103*, 07A320. [CrossRef]
57. Khabibullin, V.R.; Chetyrkina, M.R.; Obydennyy, S.I.; Maksimov, S.V.; Stepanov, G.V.; Shtykov, S.N. Study on Doxorubicin Loading on Differently Functionalized Iron Oxide Nanoparticles: Implications for Controlled Drug-Delivery Application. *Int. J. Mol. Sci.* **2023**, *24*, 4480. [CrossRef]
58. Sritharan, S.; Sivalingam, N. A Comprehensive Review on Time-Tested Anticancer Drug Doxorubicin. *Life Sci.* **2021**, *278*, 119527. [CrossRef] [PubMed]

59. Christidi, E.; Brunham, L.R. Regulated Cell Death Pathways in Doxorubicin-Induced Cardiotoxicity. *Cell Death Dis.* **2021**, *12*, 339. [CrossRef] [PubMed]
60. Wang, Y.J.; Lin, P.Y.; Hsieh, S.L.; Kirankumar, R.; Lin, H.Y.; Li, J.H.; Chen, Y.T.; Wu, H.M.; Hsieh, S. Utilizing Edible Agar as a Carrier for Dual Functional Doxorubicin-Fe_3O_4 Nanotherapy Drugs. *Materials* **2021**, *14*, 1824. [CrossRef] [PubMed]
61. Nieciecka, D.; Celej, J.; Żuk, M.; Majkowska-pilip, A.; Żelechowska-Matysiak, K.; Lis, A.; Osial, M. Hybrid System for Local Drug Delivery and Magnetic Hyperthermia Based on Spions Loaded with Doxorubicin and Epirubicin. *Pharmaceutics* **2021**, *13*, 480. [CrossRef]
62. Norouzi, M.; Yathindranath, V.; Thliveris, J.A.; Kopec, B.M.; Siahaan, T.J.; Miller, D.W. Doxorubicin-Loaded Iron Oxide Nanoparticles for Glioblastoma Therapy: A Combinational Approach for Enhanced Delivery of Nanoparticles. *Sci. Rep.* **2020**, *10*, 11292. [CrossRef]
63. Cai, W.; Guo, M.; Weng, X.; Zhang, W.; Chen, Z. Adsorption of Doxorubicin Hydrochloride on Glutaric Anhydride Functionalized Fe_3O_4@SiO_2 Magnetic Nanoparticles. *Mater. Sci. Eng. C* **2019**, *98*, 65–73. [CrossRef] [PubMed]
64. Ahmad, I.; Khan, M.F.A.; Rahdar, A.; Hussain, S.; Tareen, F.K.; Salim, M.W.; Ajalli, N.; Amirzada, M.I.; Khan, A. Design and Evaluation of PH Sensitive PEG-Protamine Nanocomplex of Doxorubicin for Treatment of Breast Cancer. *Polymers* **2022**, *14*, 2403. [CrossRef] [PubMed]
65. Rahdar, A.; Hajinezhad, M.R.; Hamishekar, H.; Ghamkhari, A.; Kyzas, G.Z. Copolymer/Graphene Oxide Nanocomposites as Potential Anticancer Agents. *Polym. Bull.* **2021**, *78*, 4877–4898. [CrossRef]
66. Mahdavinia, G.R.; Hoseinzadeh, H.; Labib, P.; Jabbari, P.; Mohebbi, A.; Barzeger, S.; Jafari, H. (Magnetic Laponite/κ-Carrageenan)@chitosan Core–Shell Carrier for pH-Sensitive Release of Doxorubicin. *Polym. Bull.* **2023**. [CrossRef]
67. Pourmadadi, M.; Ahmadi, M.J.; Dinani, H.S.; Ajalli, N.; Dorkoosh, F. Theranostic Applications of Stimulus-Responsive Systems Based on Fe_2O_3. *Pharm. Nanotechnol.* **2022**, *10*, 90–112. [CrossRef] [PubMed]
68. Hernandes, E.P.; Lazarin-Bidóia, D.; Bini, R.D.; Nakamura, C.V.; Cótica, L.F.; de Oliveira Silva Lautenschlager, S. Doxorubicin-Loaded Iron Oxide Nanoparticles Induce Oxidative Stress and Cell Cycle Arrest in Breast Cancer Cells. *Antioxidants* **2023**, *12*, 237. [CrossRef]
69. Kato, Y.; Ozawa, S.; Miyamoto, C.; Maehata, Y.; Suzuki, A.; Maeda, T.; Baba, Y. Acidic Extracellular Microenvironment and Cancer. *Cancer Cell Int.* **2013**, *13*, 89. [CrossRef] [PubMed]
70. Santhamoorthy, M.; Vy Phan, T.T.; Ramkumar, V.; Raorane, C.J.; Thirupathi, K.; Kim, S.C. Thermo-Sensitive Poly (N-Isopropylacrylamide-Co-Polyacrylamide) Hydrogel for PH-Responsive Therapeutic Delivery. *Polymers* **2022**, *14*, 4128. [CrossRef] [PubMed]
71. Ding, H.; Inoue, S.; Ljubimov, A.V.; Patil, R.; Portilla-Arias, J.; Hu, J.; Konda, B.; Wawrowsky, K.A.; Fujita, M.; Karabalin, N.; et al. Inhibition of Brain Tumor Growth by Intravenous Poly (β-L-Malic Acid) Nanobioconjugate with PH-Dependent Drug Release. *Proc. Natl. Acad. Sci. USA* **2010**, *107*, 18143–18148. [CrossRef] [PubMed]
72. Kovrigina, E.; Chubarov, A.; Dmitrienko, E. High Drug Capacity Doxorubicin-Loaded Iron Oxide Nanocomposites for Cancer Therapy. *Magnetochemistry* **2022**, *8*, 54. [CrossRef]
73. Wang, H.T.; Chou, P.C.; Wu, P.H.; Lee, C.M.; Fan, K.H.; Chang, W.J.; Lee, S.Y.; Huang, H.M. Physical and Biological Evaluation of Low-Molecular-Weight Hyaluronic Acid/Fe_3O_4 Nanoparticle for Targeting MCF7 Breast Cancer Cells. *Polymers* **2020**, *12*, 1094. [CrossRef]
74. Mosmann, T. Rapid Colorimetric Assay for Cellular Growth and Survival: Application to Proliferation and Cytotoxicity Assays. *J. Immunol. Methods* **1983**, *65*, 55–63. [CrossRef] [PubMed]
75. Mahdavi, M.; Bin Ahmad, M.; Haron, M.J.; Namvar, F.; Nadi, B.; Ab Rahman, M.Z.; Amin, J. Synthesis, Surface Modification and Characterisation of Biocompatible Magnetic Iron Oxide Nanoparticles for Biomedical Applications. *Molecules* **2013**, *18*, 7533–7548. [CrossRef]
76. Yallapu, M.M.; Foy, S.P.; Jain, T.K.; Labhasetwar, V. PEG-Functionalized Magnetic Nanoparticles for Drug Delivery and Magnetic Resonance Imaging Applications. *Pharm. Res.* **2010**, *27*, 2283–2295. [CrossRef]
77. Shete, P.B.; Patil, R.M.; Tiwale, B.M.; Pawar, S.H. Water Dispersible Oleic Acid-Coated Fe_3O_4 Nanoparticles for Biomedical Applications. *J. Magn. Magn. Mater.* **2015**, *377*, 406–410. [CrossRef]
78. Niu, Y.Q.; Liu, J.H.; Aymonier, C.; Fermani, S.; Kralj, D.; Falini, G.; Zhou, C.H. Calcium Carbonate: Controlled Synthesis, Surface Functionalization, and Nanostructured Materials. *Chem. Soc. Rev.* **2022**, *51*, 7883–7943. [CrossRef] [PubMed]
79. Jiao, W.; Zhang, T.; Peng, M.; Yi, J.; He, Y.; Fan, H. Design of Magnetic Nanoplatforms for Cancer Theranostics. *Biosensors* **2022**, *12*, 38. [CrossRef] [PubMed]
80. Ching, Y.C.; Gunathilake, T.M.S.U.; Chuah, C.H.; Ching, K.Y.; Singh, R.; Liou, N.S. Curcumin/Tween 20-Incorporated Cellulose Nanoparticles with Enhanced Curcumin Solubility for Nano-Drug Delivery: Characterization and in Vitro Evaluation. *Cellulose* **2019**, *26*, 5467–5481. [CrossRef]
81. Huang, Y.; Zhang, B.; Xie, S.; Yang, B.; Xu, Q.; Tan, J. Superparamagnetic Iron Oxide Nanoparticles Modified with Tween 80 Pass through the Intact Blood-Brain Barrier in Rats under Magnetic Field. *ACS Appl. Mater. Interfaces* **2016**, *8*, 11336–11341. [CrossRef]
82. Ayub, A.; Wettig, S. An Overview of Nanotechnologies for Drug Delivery to the Brain. *Pharmaceutics* **2022**, *14*, 224. [CrossRef] [PubMed]

83. Vergaro, V.; Pisano, I.; Grisorio, R.; Baldassarre, F.; Mallamaci, R.; Santoro, A.; Suranna, G.P.; Papadia, P.; Fanizzi, F.P.; Ciccarella, G. $CaCO_3$ as an Environmentally Friendly Renewable Material for Drug Delivery Systems: Uptake of HSA-$CaCO_3$ Nanocrystals Conjugates in Cancer Cell Lines. *Materials* **2019**, *12*, 1481. [CrossRef]
84. Bondarenko, L.; Terekhova, V.; Kahru, A.; Dzhardimalieva, G.; Kelbysheva, E.; Tropskaya, N.; Kydralieva, K. Sample Preparation Considerations for Surface and Crystalline Properties and Ecotoxicity of Bare and Silica-Coated Magnetite Nanoparticles. *RSC Adv.* **2021**, *11*, 32227–32235. [CrossRef]
85. Ibarra, J.; Melendres, J.; Almada, M.; Burboa, M.G.; Taboada, P.; Juárez, J.; Valdez, M.A. Synthesis and Characterization of Magnetite/PLGA/Chitosan Nanoparticles. *Mater. Res. Express* **2015**, *2*, 95010. [CrossRef]
86. Rodriguez-Blanco, J.D.; Shaw, S.; Benning, L.G. The Kinetics and Mechanisms of Amorphous Calcium Carbonate (ACC) Crystallization to Calcite, via Vaterite. *Nanoscale* **2011**, *3*, 265–271. [CrossRef] [PubMed]
87. Bin Cai, G.; Chen, S.F.; Liu, L.; Jiang, J.; Bin Yao, H.; Xu, A.W.; Yu, S.H. 1,3-Diamino-2-Hydroxypropane-N,N,N′,N′-Tetraacetic Acid Stabilized Amorphous Calcium Carbonate: Nucleation, Transformation and Crystal Growth. *CrystEngComm* **2010**, *12*, 234–241. [CrossRef]
88. Bansal, R.; Singh, R.; Kaur, K. Quantitative Analysis of Doxorubicin Hydrochloride and Arterolane Maleate by Mid IR Spectroscopy Using Transmission and Reflectance Modes. *BMC Chem.* **2021**, *15*, 1–11. [CrossRef]
89. Liang, J.; Yang, X.; Liu, D.; Cong, M.; Song, Y.; Bai, S. Lipid/Hyaluronic Acid–Coated Doxorubicin-Fe_3O_4 as a Dual-Targeting Nanoparticle for Enhanced Cancer Therapy. *AAPS PharmSciTech* **2020**, *21*, 1–9. [CrossRef] [PubMed]
90. Lin, J.; Huang, L.; Xiang, R.; Ou, H.; Li, X.; Chen, A.; Liu, Z. Blood Compatibility Evaluations of $CaCO_3$ Particles. *Biomed. Mater.* **2021**, *16*, 055010. [CrossRef]
91. Nigam, S.; Chandra, S.; Newgreen, D.F.; Bahadur, D.; Chen, Q. Poly(Ethylene Glycol)-Modified PAMAM-Fe_3O_4- Doxorubicin Triads with the Potential for Improved Therapeutic Efficacy: Generation-Dependent Increased Drug Loading and Retention at Neutral PH and Increased Release at Acidic PH. *Langmuir* **2014**, *30*, 1004–1011. [CrossRef] [PubMed]
92. Ibiyeye, K.M.; Nordin, N.; Ajat, M.; Zuki, A.B.Z. Ultrastructural Changes and Antitumor Effects of Doxorubicin/Thymoquinone-Loaded $CaCO_3$ Nanoparticles on Breast Cancer Cell Line. *Front. Oncol.* **2019**, *9*, 599. [CrossRef]
93. Vidallon, M.L.P.; Douek, A.M.; Quek, A.; McLiesh, H.; Kaslin, J.; Tabor, R.F.; Bishop, A.I.; Teo, B.M. Gas-Generating, PH-Responsive Calcium Carbonate Hybrid Particles with Biomimetic Coating for Contrast-Enhanced Ultrasound Imaging. *Part. Part. Syst. Charact.* **2020**, *37*, 1900471. [CrossRef]
94. Halder, K.; Sengupta, P.; Chaki, S.; Saha, R.; Dasgupta, S. Understanding Conformational Changes in Human Serum Albumin and Its Interactions with Gold Nanorods: Do Flexible Regions Play a Role in Corona Formation? *Langmuir* **2022**, *39*, 1651–1664. [CrossRef]
95. Corbo, C.; Molinaro, R.; Parodi, A.; Toledano Furman, N.E.; Salvatore, F.; Tasciotti, E. The Impact of Nanoparticle Protein Corona on Cytotoxicity, Immunotoxicity and Target Drug Delivery. *Nanomedicine* **2016**, *11*, 81–100. [CrossRef]
96. Rampado, R.; Crotti, S.; Caliceti, P.; Pucciarelli, S.; Agostini, M. Recent Advances in Understanding the Protein Corona of Nanoparticles and in the Formulation of "Stealthy" Nanomaterials. *Front. Bioeng. Biotechnol.* **2020**, *8*, 166. [CrossRef]
97. Hasan, M.; Zafar, A.; Jabbar, M.; Tariq, T.; Manzoor, Y.; Mahmood, M.; Hassan, S.G.; Shu, X.; Mahmood, N. Trident Nano-Indexing the Proteomics Table: Next Version Clustering of Iron Carbide NPs and Protein Corona. *Molecules* **2022**, *27*, 5754. [CrossRef] [PubMed]
98. Saptarshi, S.R.; Duschl, A.; Lopata, A.L. Interaction of Nanoparticles with Proteins: Relation to Bio-Reactivity of the Nanoparticle. *J. Nanobiotechnol.* **2013**, *11*, 12–26. [CrossRef] [PubMed]
99. Simon, J.; Kuhn, G.; Fichter, M.; Gehring, S.; Landfester, K.; Mailänder, V. Unraveling the in Vivo Protein Corona. *Cells* **2021**, *10*, 132. [CrossRef] [PubMed]
100. Chubarov, A.; Spitsyna, A.; Krumkacheva, O.; Mitin, D.; Suvorov, D.; Tormyshev, V.; Fedin, M.; Bowman, M.K.; Bagryanskaya, E. Reversible Dimerization of Human Serum Albumin. *Molecules* **2021**, *26*, 108. [CrossRef]
101. Dobrynin, S.; Kutseikin, S.; Morozov, D.; Krumkacheva, O.; Spitsyna, A.; Gatilov, Y.; Silnikov, V.; Angelovski, G.; Bowman, M.K.; Kirilyuk, I.; et al. Human Serum Albumin Labelled with Sterically-Hindered Nitroxides as Potential MRI Contrast Agents. *Molecules* **2020**, *25*, 1709. [CrossRef]
102. Lisitskiy, V.A.; Khan, H.; Popova, T.V.; Chubarov, A.S.; Zakharova, O.D.; Akulov, A.E.; Shevelev, O.B.; Zavjalov, E.L.; Koptyug, I.V.; Moshkin, M.P.; et al. Multifunctional Human Serum Albumin-Therapeutic Nucleotide Conjugate with Redox and PH-Sensitive Drug Release Mechanism for Cancer Theranostics. *Bioorganic Med. Chem. Lett.* **2017**, *27*, 3925–3930. [CrossRef] [PubMed]
103. Popova, T.V.; Khan, H.; Chubarov, A.S.; Lisitskiy, V.A.; Antonova, N.M.; Akulov, A.E.; Shevelev, O.B.; Zavjalov, E.L.; Silnikov, V.N.; Ahmad, S.; et al. Biotin-Decorated Anti-Cancer Nucleotide Theranostic Conjugate of Human Serum Albumin: Where the Seed Meets the Soil? *Bioorganic Med. Chem. Lett.* **2018**, *28*, 260–264. [CrossRef]
104. Chubarov, A.S.; Zakharova, O.D.; Koval, O.A.; Romaschenko, A.V.; Akulov, A.E.; Zavjalov, E.L.; Razumov, I.A.; Koptyug, I.V.; Knorre, D.G.; Godovikova, T.S. Design of Protein Homocystamides with Enhanced Tumor Uptake Properties for 19F Magnetic Resonance Imaging. *Bioorg. Med. Chem.* **2015**, *23*, 6943–6954. [CrossRef] [PubMed]
105. Chubarov, A.S.; Shakirov, M.M.; Koptyug, I.V.; Sagdeev, R.Z.; Knorre, D.G.; Godovikova, T.S. Synthesis and Characterization of Fluorinated Homocysteine Derivatives as Potential Molecular Probes for 19F Magnetic Resonance Spectroscopy and Imaging. *Bioorg. Med. Chem. Lett.* **2011**, *21*, 4050–4053. [CrossRef] [PubMed]

106. Mariam, J.; Sivakami, S.; Dongre, P.M. Albumin Corona on Nanoparticles–a Strategic Approach in Drug Delivery. *Drug Deliv.* **2016**, *23*, 2668–2676. [CrossRef]
107. Yallapu, M.M.; Chauhan, N.; Othman, S.F.; Khalilzad-Sharghi, V.; Ebeling, M.C.; Khan, S.; Jaggi, M.; Chauhan, S.C. Implications of Protein Corona on Physico-Chemical and Biological Properties of Magnetic Nanoparticles. *Biomaterials* **2015**, *46*, 1–12. [CrossRef] [PubMed]
108. Sakulkhu, U.; Mahmoudi, M.; Maurizi, L.; Salaklang, J.; Hofmann, H. Protein Corona Composition of Superparamagnetic Iron Oxide Nanoparticles with Various Physico-Chemical Properties and Coatings. *Sci. Rep.* **2014**, *4*, 5020. [CrossRef] [PubMed]
109. Moya, C.; Escudero, R.; Malaspina, D.C.; De La Mata, M.; Hernández-Saz, J.; Faraudo, J.; Roig, A. Insights into Preformed Human Serum Albumin Corona on Iron Oxide Nanoparticles: Structure, Effect of Particle Size, Impact on MRI Efficiency, and Metabolization. *ACS Appl. Bio Mater.* **2019**, *2*, 3084–3094. [CrossRef] [PubMed]